

The supermassive black hole of Fornax A^{*}

N. Nowak^{1,2}†, R. P. Saglia^{1,2}, J. Thomas^{1,2}, R. Bender^{1,2}, R. I. Davies¹, K. Gebhardt³

¹*Max-Planck-Institut für extraterrestrische Physik, Giessenbachstrasse, 85748 Garching, Germany*

²*Universitätssternwarte, Scheinerstrasse 1, 81679 München, Germany*

³*Astronomy Department, University of Texas, Austin, TX 78723*

Received 2008 August 22; in original form 2008 July 19

ABSTRACT

The radio galaxy Fornax A (NGC 1316) is a prominent merger remnant in the outskirts of the Fornax cluster. Its giant radio lobes suggest the presence of a powerful AGN, and thus a central supermassive black hole (SMBH). Fornax A now seems to be in a transition state between active black hole growth and quiescence, as indicated by the strongly declined activity of the nucleus. Studying objects in this evolutionary phase is particularly important in order to understand the link between bulge formation and black hole growth, which is manifested in the M_{\bullet} - σ relation between black hole mass and bulge velocity dispersion. So far a measurement of the SMBH mass has not been possible in Fornax A, as it is enshrouded in dust which makes optical measurements impossible. We present high-resolution adaptive optics assisted integral-field data of Fornax A, taken with SINFONI at the Very Large Telescope in the K band, where the influence of dust is negligible. The achieved spatial resolution is 0.085 arcsec, which is about a fifth of the diameter of the expected sphere of influence of the black hole. The stellar kinematics was measured using the region around the CO bandheads at 2.3 μm . Fornax A does not rotate inside the inner ~ 3 arcsec. The velocity dispersion increases towards the centre. The weak AGN emission affects the stellar kinematics in the inner ~ 0.06 arcsec only. Beyond this radius, the stellar kinematics appears relaxed in the central regions. We use axisymmetric orbit models to determine the mass of the SMBH in the centre of Fornax A. The three-dimensional nature of our data provides the possibility to directly test the consistency of the data with axisymmetry by modelling each of the four quadrants separately. According to our dynamical models, consistent SMBH masses M_{\bullet} and dynamical Ks band mass-to-light ratios Υ are obtained for all quadrants, with $\langle M_{\bullet} \rangle = 1.3 \times 10^8 M_{\odot}$ ($\text{rms}(M_{\bullet}) = 0.4 \times 10^8 M_{\odot}$) and $\langle \Upsilon \rangle = 0.68$ ($\text{rms}(\Upsilon) = 0.03$), confirming the assumption of axisymmetry. For the folded and averaged data we find $M_{\bullet} = 1.5_{-0.8}^{+0.75} \times 10^8 M_{\odot}$ and $\Upsilon = 0.65_{-0.05}^{+0.075}$ (3σ errors). Thus the black-hole mass of Fornax A is consistent within the error with the Tremaine et al. (2002) M_{\bullet} - σ relation, but is a factor ~ 4 smaller than expected from its bulge mass and the Marconi & Hunt (2003) relation.

Key words: galaxies: individual: NGC 1316 (Fornax A) – galaxies: kinematics and dynamics.

1 INTRODUCTION

Studies of the dynamics of stars and gas in the centres of nearby galaxies with a massive bulge component have established the presence of supermassive black holes (SMBHs) in the 10^6 – $10^9 M_{\odot}$ range. The mass of the central SMBH is

tightly correlated with the bulge mass or luminosity (e.g. Marconi & Hunt 2003) and with the bulge velocity dispersion σ (Gebhardt et al. 2000b; Ferrarese & Merritt 2000). These correlations suggest that bulge evolution and black hole growth are closely linked. Indeed there is increasing theoretical evidence that galaxy merging (or other processes that lead to gas inflow, like secular evolution), nuclear activity and feedback are all somehow linked to bulge and SMBH evolution (e.g. Di Matteo et al. 2005; Johansson et al. 2008; Younger et al. 2008; Hopkins et al. 2008). To observationally constrain present theories of bulge and black hole evolution, detailed studies of AGN and merger remnants in differ-

* Based on observations at the European Southern Observatory VLT (076.B-0457(A)) and archival ESO La Silla (66.C-0310(A)) and NASA/ESA *Hubble Space Telescope* data (GO Proposal 7458), obtained from the ESO/ST-ECF Science Archive Facility † E-mail: nnowak@mpe.mpg.de

ent evolutionary stages are essential. NGC 5128 (Cen A) is presently the only galaxy with a powerful AGN that underwent a recent major merger which has a measured black-hole mass (Silge et al. 2005; Marconi et al. 2006; Neumayer et al. 2007).

A galaxy very similar to Cen A is NGC 1316 (Fornax A). Fornax A is a giant elliptical galaxy located in the outskirts of the Fornax galaxy cluster. It is one of the brightest radio galaxies in the sky with giant double radio lobes and S-shaped nuclear radio jets (Geldzahler & Fomalont 1984). The peculiar morphology with numerous tidal tails, shells and loops (Schweizer 1980, 1981) suggests that a major merger happened about 3 Gyr ago (Goudfrooij et al. 2001), followed by some minor mergers (Mackie & Fabbiano 1998). Its nucleus however is surprisingly faint in X-rays, which can only be explained if the nucleus became dormant during the last 0.1 Gyr (Iyomoto et al. 1998). This makes it an ideal target for a dynamical black-hole mass measurement, as its stellar absorption lines are probably not or just marginally diluted by non-stellar emission from the AGN.

Fornax A is classified as an intermediate form between core and power law galaxy in Lauer et al. (2007). The surface brightness approximately follows an $r^{1/4}$ -law (Caon et al. 1994). Large amounts of dust are present also in the inner few arcseconds, which affects optical spectroscopy. We therefore measure the two-dimensional stellar kinematics of Fornax A with the near-infrared integral-field spectrograph SINFONI at the Very Large Telescope (VLT) in the *K* band, where the dust obscuration is only about 7 per cent of the obscuration in the optical. We use this data to analyse the stellar kinematics in a way similar to Nowak et al. (2007).

Throughout this paper we adopt a distance to Fornax A of 18.6 Mpc based on *HST* measurements of Cepheid variables in NGC 1365 (Madore et al. 1999). At this distance, 1 arcsec corresponds to 90 pc. With a velocity dispersion of 226 km s^{-1} (mean σ measured in an 8 arcsec aperture in §3.4) the estimated sphere of influence has a diameter of 0.46 arcsec and we would expect a SMBH mass of $2.2 \times 10^8 M_{\odot}$ (Tremaine et al. 2002). This is large enough to be resolved easily from the ground with adaptive optics.

This paper is organized as follows: In §2 we present the data and the data reduction. The stellar kinematics of Fornax A is described in §3, the measurement of the near-infrared line strength indices in §4. The stellar dynamical modelling procedure and the results for the SMBH mass are presented in §5, and §6 summarises and discusses the results.

2 DATA & DATA REDUCTION

2.1 SINFONI data

Fornax A was observed between 2005 October 10 and 12 as part of guaranteed time observations with SINFONI (Eisenhauer et al. 2003; Bonnet et al. 2004), an adaptive-optics assisted integral-field spectrograph at the VLT UT4. The nucleus of Fornax A served as guide star for the AO correction. We used the *K* band grating ($1.95 - 2.45 \mu\text{m}$) and, depending on the seeing conditions, the intermediate size field of view of 3×3 arcsec (0.05×0.1 arcsec spaxel^{-1} , referred to as “100mas scale” in the following) or the high resolution mode with a 0.8×0.8 arcsec field of view (0.0125×0.025 arcsec spaxel^{-1} , “25mas scale”). The total on-source exposure

time was 130 min in the highest resolution mode and 70 min using the intermediate plate scale, consisting of 10 min exposures taken in series of “object–sky–object” (O–S–O) cycles, dithered by up to 0.2 arcsec. In addition three O–S–O cycles of 5 min exposure time each were taken using the low resolution mode (8×8 arcsec field of view, “250mas scale”).

The SINFONI data reduction package SPRED (Schreiber et al. 2004; Abuter et al. 2006) was used to reduce the data. It includes all common reduction steps necessary for near-infrared (near-IR) data plus routines to reconstruct the three-dimensional datacubes. The data were skysubtracted, flatfielded, corrected for bad pixels and for distortion and then wavelength calibrated using a Ne/Ar lamp frame. The wavelength calibration was corrected using night-sky lines if necessary. Then the datacubes were reconstructed and corrected for atmospheric absorption using B stars that do not have strong spectral features in the region of the CO bandheads. As a final step all datacubes were averaged together to produce the final datacube. The data of the telluric stars were reduced likewise. The flux calibration of the 250mas data was performed by comparison to the photometrically calibrated NTT/SOFI *Ks* band imaging (see §2.3 and Fig. 3), that gives a *Ks* magnitude of 8.44 in an 8 arcsec aperture. The 100mas image was calibrated with respect to the 250mas image and the 25mas image with respect to the 100mas image. Fig. 1 shows the resulting image of Fornax A in all three platescales, collapsed along the wavelength direction within the SOFI *Ks* band region.

The spatial resolution, i.e. the FWHM of the point-spread function (PSF), is difficult to derive when dealing with high-resolution AO observations of diffuse objects. Deriving it from the science data itself can work quite well, if there are either stars in the field of view or the target is an AGN or starburst galaxy with certain spectral properties (see e.g. Mueller Sánchez et al. 2006; Davies et al. 2006, 2007). None of this applies to Fornax A. Therefore we derived the PSF by regularly taking an exposure of a nearby star with approximately the same *R* band magnitude and *B* – *R* colour as the central 3 arcsec of Fornax A. This procedure is usually recommended to observers, but apart from being very time-consuming it can also be unreliable under certain conditions (Davies et al. 2004). The atmosphere may vary strongly with time, resulting in a measured PSF that is different from the real one. In addition the response of the wavefront sensor to the PSF star is, to some degree, different from the response to the AO guide star (the nucleus in this case), because the nucleus is extended and therefore the flux distribution on the wavefront sensor is different. We used this method as it was the only available option to measure the PSF.

The high-resolution (25mas) data were taken under good and relatively stable ambient conditions with a near-IR seeing around 0.6 arcsec. The two-dimensional PSF (i.e. the image of the PSF reference star) is shown in Fig. 2a. The spatial resolution is $\text{FWHM} \approx 0.085$ arcsec. A Strehl ratio of ≈ 45 per cent was reached. The reliability of this PSF is verified by a comparison of the 25mas SINFONI luminosity profile with an *HST*/NICMOS F160W (camera NIC2, sampled at 0.075 arcsec px^{-1}) luminosity profile. They agree well without further broadening of the NICMOS data (see below and Fig. 4).

During the hours of degraded seeing (around ≈ 0.9 arc-

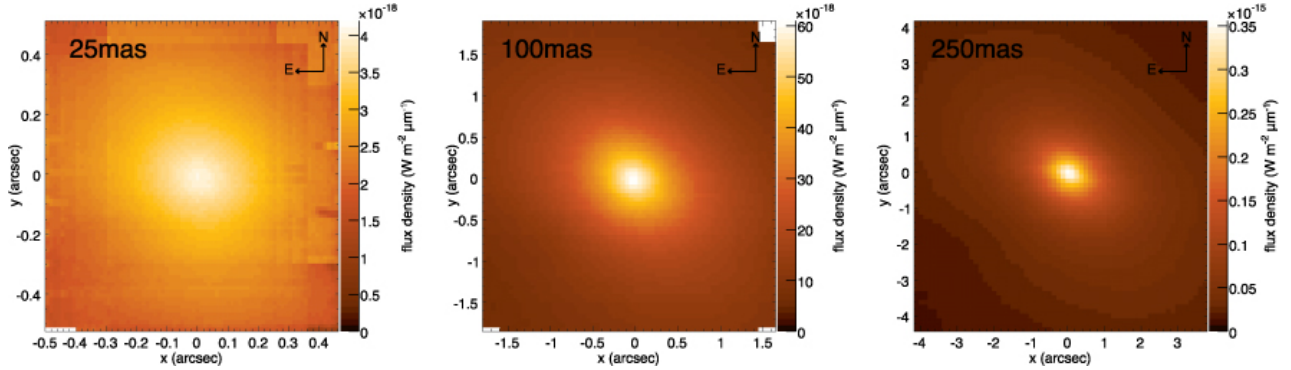


Figure 1. SINFONI images of Fornax A in the 25mas (left), 100mas (middle) and 250mas (right) scale.

sec on average in the near-IR) on October 12 we observed Fornax A using the intermediate plate scale (100mas). The spatial resolution inferred from the PSF is ≈ 0.16 arcsec and the achieved Strehl ratio was ≈ 18 per cent. The shape of the PSF (Fig. 2b) is rather asymmetric and may not represent the true PSF due to the changeable weather conditions. The seeing and the coherence time drastically improved during the observations with the 100mas scale, so we switched to the 25mas scale for approximately one hour and only when the seeing and the coherence time then degraded again to similar values as before we could observe the 100mas PSF. In order to get a better estimate of the real PSF we computed the kernel that transforms the 25mas image of Fornax A (binned 4×4 to match the 100mas spaxel size) into the 100mas image using the program of Gössl & Riffeser (2002). The 25mas PSF was then rebinned to the 100mas spaxel size and convolved with this kernel. Kernel and resulting PSF are shown in Fig. 2c and 2d. The shape of the kernel and hence the convolved PSF are quite noisy. The reason is the low S/N of the 25mas image compared to the 100mas image (cf. Fig. 1). In order to find the closest match between the two images the kernel tries to incorporate the noise, too. Thus the resulting PSF has a S/N more similar to the 25mas image than to the image of a bright PSF star. Nevertheless the convolved PSF has about the same FWHM as the measured 100mas PSF star.

The PSF is an integral part of the dynamical modelling and it is therefore important to know its shape as accurate as possible. However, so far no studies have been performed that analyse systematically the dependence of the resulting M_{\bullet} and mass-to-light ratio on the PSF shape. Such a study is beyond the scope of this paper, nevertheless we will do the modelling, as far as 100mas data are included, twice, using one time the measured PSF and the other time the convolved PSF.

2.2 Longslit data

Kinematics derived from longslit spectra are useful to constrain the orbital structure at large radii, outside the small SINFONI field of view. Major-axis longslit data of Fornax A are available from different authors (Longhetti et al. 1998; Arnaboldi et al. 1998; Bedregal et al. 2006; Saglia et al. 2002). Longhetti et al. (1998) and Arnaboldi et al. (1998) measured only v and σ from optical absorption lines (Mgb) and from the CaT region in the near-IR, they did not mea-

sure the higher-order Gauss–Hermite coefficients h_3 and h_4 (Gerhard 1993; van der Marel & Franx 1993) which quantify asymmetric and symmetric deviations from a Gaussian velocity profile. Bedregal et al. (2006) measured all four parameters from optical spectra, whereas Saglia et al. (2002) used the CaT region. The velocities of all measurements are consistent, taking into account the different seeing values. The velocity dispersions in the central ~ 5 arcsec however range from ≈ 220 km s $^{-1}$ to ≈ 260 km s $^{-1}$. The reasons for that can be diverse. The authors used different correlation techniques, different spectral lines and slightly different position angles. Fornax A contains dust, which might alter the kinematics measured from optical absorption lines. Silge & Gebhardt (2003) found that optical dispersions tend to be larger than those measured from the CO bandheads, which could be an effect of dust. The largest dispersions are indeed those measured from optical spectra. We therefore used the kinematics of Saglia et al. (2002), as they measured all four parameters from the CaT line region. Their measurements agree best with our SINFONI measurements. They observed Fornax A in October 2001 at the Siding Spring 2.3m telescope using a 6.7 arcmin \times 4 arcsec longslit and an exposure time of 60 min and determined the kinematics with the Fourier Correlation Quotient method (Bender et al. 1994). As they assume a position angle of 58° we adopt this value in the following analysis. The major axis profiles are shown in Fig. 17 and in Beletsky et al. (2008).

2.3 Imaging

To measure the SMBH mass in Fornax A, it is essential to determine the gravitational potential made up by the stellar component using photometric measurements with sufficient spatial resolution and radial extent. Therefore we combine high-resolution *HST* NICMOS F160W and ground-based wide-field *Ks* band imaging. The low-resolution *Ks* band image was taken with the near-IR imager/spectrometer SOFI on the 3.5m NTT telescope on La Silla, Chile. It has a field of view of 4.9×4.9 arcmin with 0.29 arcsec px $^{-1}$ and a seeing of ~ 0.7 arcsec. It was dust-corrected with the method described in Appendix A using a *J* band SOFI image. The dust-corrected image is shown in Fig. 3. Note that the original SOFI image and the residuals are shown in Beletsky et al. (2008). We applied the same method to the *HST* NICMOS F160W image, which we corrected using a NICMOS F110W image. The isophotal profiles of the dust-

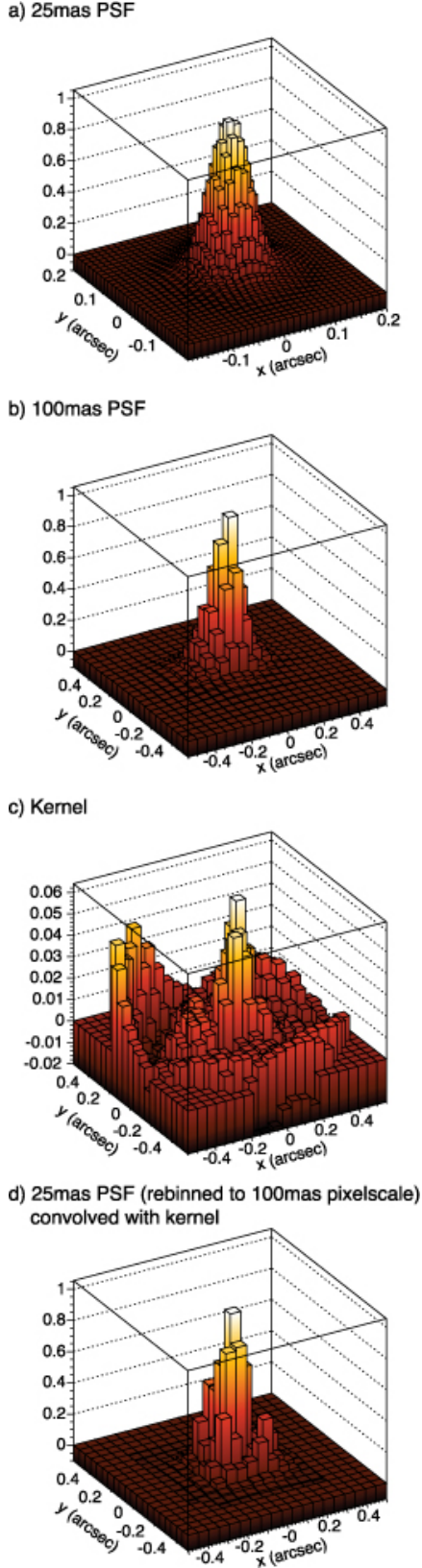


Figure 2. a) 25mas PSF derived by observing a star of about the same magnitude and colour as the AO guide star (i.e. the nucleus of Fornax A) during the observations. b) Same as (a) but for the 100mas scale. c) Kernel that transforms the 25mas image of Fornax A to the 100mas image. d) 25mas PSF from (a) rebinned to the 100mas spaxel size and convolved with the kernel from (c).

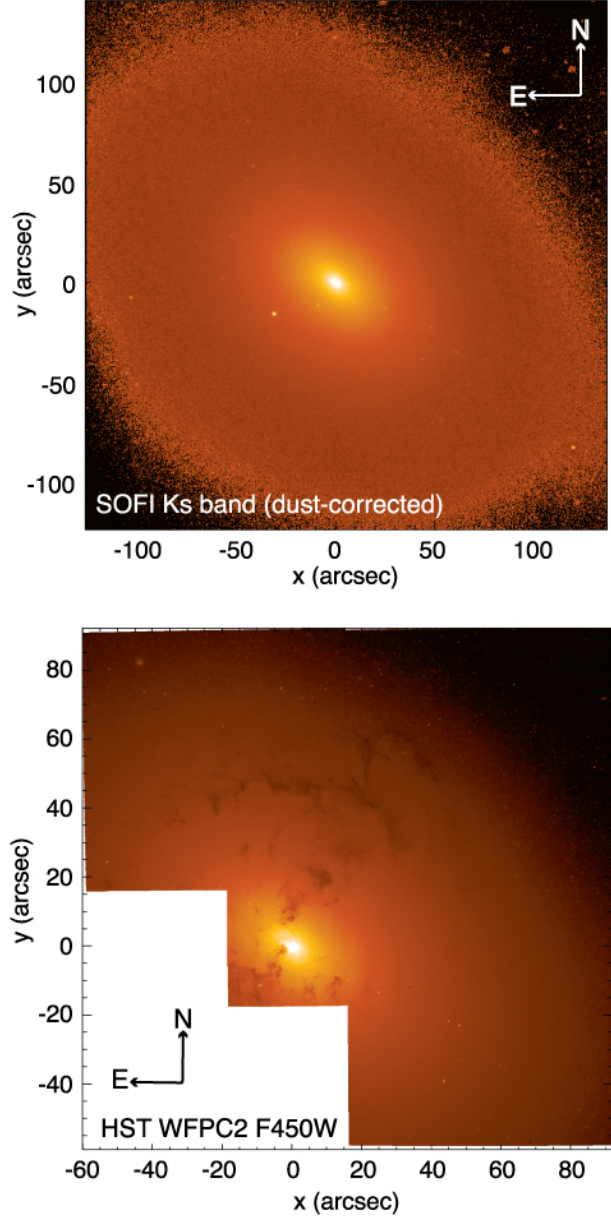


Figure 3. The top panel shows the dust-corrected SOFI *Ks* band image of Fornax A (courtesy Y. Beletsky). The dust-corrected light distribution appears very smooth and regular and the isophotes are slightly boxy. For comparison the *HST* WFPC2 F450W image (NASA/ESA *HST* data (GO Proposal 5990), obtained from the ESO/ST-ECF Science Archive Facility), which highlights the strong dust lanes, is presented in the bottom panel.

corrected images were obtained following Bender & Moellenhoff (1987). The light distribution appears very smooth and regular and the isophotes are slightly boxy. The surface brightness profiles were then combined using the method of Corsini et al. (2008), matching the profiles in the region between 1.5 arcsec and 5.0 arcsec and shifting the NICMOS profile by the computed amount ($\mu_{\text{SOFI}} - \mu_{\text{HST}}$) on to the *Ks* band SOFI profile. The original and the combined profiles are shown in Fig. 4.

The combined photometry extends out to 80 arcsec and was deprojected for an inclination $i = 90^\circ$ using the program

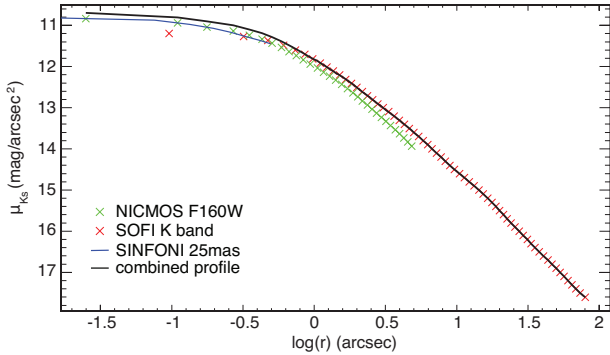


Figure 4. Surface brightness profiles of the *HST* NICMOS dust-corrected *H* band image (green crosses), the SOFI dust corrected *K_s* band image (red crosses) and the combination of the two surface brightness profiles (black line). The SINFONI 25mas *K* band image (scaled to match the *HST* NICMOS profile) is overplotted in blue.

of Magorrian (1999) under the assumption that the galaxy is axisymmetric. No shape penalty was applied. The stellar mass density then can be modelled via $\rho_* = \Upsilon\nu$, where ν is the luminosity density obtained from the deprojection. The *K_s* band mass-to-light ratio Υ is assumed to be constant with radius. This assumption holds approximately in the central part of the galaxy for which we have kinematic data and where dark matter does not play a major role.

3 STELLAR KINEMATICS

The stellar kinematic information are extracted using the maximum penalised likelihood (MPL) technique of Gebhardt et al. (2000a), which obtains non-parametric line-of-sight velocity distributions (LOSVDs) as follows: an initial binned velocity profile is convolved with a linear combination of template spectra and the residuals of the resulting spectrum to the observed galaxy spectrum are calculated. The velocity profile is then changed successively and the weights of the templates are adjusted in order to optimise the fit to the observed spectrum by minimizing the function $\chi^2_P = \chi^2 + \alpha\mathcal{P}$, where α is the smoothing parameter that determines the level of regularisation, and the penalty function \mathcal{P} is the integral of the square of the second derivative of the LOSVD. We fitted only the first two bandheads $^{12}\text{CO}(2-0)$ and $^{12}\text{CO}(3-1)$, i.e. the spectral range between 2.275 μm and 2.349 μm rest frame wavelength. The higher-order bandheads are strongly disturbed by residual atmospheric features. At wavelengths $\lambda < 2.29 \mu\text{m}$ most absorption lines are weak such that extremely high S/N spectra would be needed. The strongest absorption line in that regime is Na I, but as its strength is much higher in early-type galaxies than in single stars due to enhanced silicon (Silva et al. 2008) it cannot be fitted by the template spectra.

3.1 Initial parameters

Before being able to obtain the final LOSVDs it is necessary to quantify possible systematic offsets and to constrain the best initial values for the smoothing parameter and the

width of the LOSVD bins for the given dataset (wavelength range, σ , h_3 , h_4 , S/N, spectral resolution). Especially the selection of the smoothing parameter α is a crucial step (Merritt 1997; Joseph et al. 2001). If α is chosen too high, the LOSVD is biased toward a flatter shape and if it is too small the LOSVD is too noisy. In order to find the best initial values for the Fornax A data Monte Carlo simulations on a large set of model galaxy spectra have been performed. These are described in detail in Appendix B.

Based on the simulations we conclude that with MPL reliable LOSVDs can be obtained from the first two CO bandheads of the SINFONI data of Fornax A when the chosen α is between 1 and 10 and the S/N $\gtrsim 30$. The S/N of our data is very high (on average ~ 70 for the 25mas and the 250mas data, and ~ 140 for the 100mas data). We are using $\alpha = 8$ for the 25mas and 250mas data and $\alpha = 6$ for the 100mas data.

3.2 Kinematic template stars

We built up a small library of late-type (K and M) kinematic template stars which were observed with SINFONI in the *K* band during commissioning and GTO observations between 2004 and 2006. In total we have nine kinematic templates for the 25mas scale (spectral resolving power $R \approx 5000$), twelve templates for the 100mas scale ($R \approx 4500$) and ten templates for the 250mas scale ($R \approx 4000$). As shown in Silge & Gebhardt (2003) a correct value of the velocity dispersion σ can only be obtained from fits to the CO bandheads, if the template has about the same intrinsic CO equivalent width (EW) as the galaxy. The CO EWs of the Fornax A spectra were measured using the definition and the velocity dispersion correction of Silge & Gebhardt (2003). The resulting values are between 13.0 \AA and 14.5 \AA .

After excluding all stellar templates with EWs far below or above the measured range, five templates remained for the 25mas scale, five for the 100mas scale and four for the 250mas scale. As a cross-check and to avoid template mismatching the kinematics was extracted first with single templates. The results agreed, so no other template star had to be excluded from the sample. Tab. 1 shows the used kinematic template stars with the according spectral types and CO EWs. For a better comparison with the line strength indices discussed in §4 the CO EWs were also measured using the definition of Silva et al. (2008).

3.3 Error estimation

The uncertainties on the velocity profiles are estimated using Monte Carlo simulations (Gebhardt et al. 2000a). A galaxy spectrum is created by convolving the template spectrum with the measured LOSVD. Then 100 realisations of that initial galaxy spectrum are created by adding appropriate Gaussian noise. The LOSVDs of each realisation are determined and used to specify the confidence intervals.

3.4 The kinematics of Fornax A

The SINFONI data are binned using a similar binning scheme as in Nowak et al. (2007) with five angular bins per quadrant and a number of radial bins (seven for the 25mas

Table 1. CO equivalents widths of the stellar kinematic template stars.

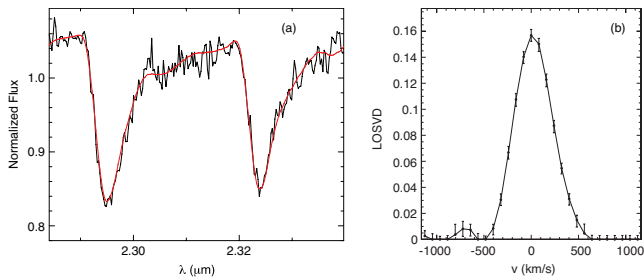
Name	spectral type	CO ^a	CO ^b	scale
HD12642	K5 III	12.7	17.09	25
HD163755	K5/M0 III	15.6	21.27	25
HD179323	K2 III	11.1	14.08	25
HD198357	K3 III	10.8	13.84	25
HD75022	K2/3 III	12.0	15.06	25, 100
HD141665	M5 III	15.8	22.26	100, 250
HD181109	K5/M0 III	12.9	17.79	100, 250
HD201901	K3 III	11.4	14.43	100, 250
SA112-0595 ^c	M0 III	12.8	17.61	100, 250

Note. The CO equivalent widths are given in units of Å. The spectral types are taken from Wright et al. (2003) where available. In the last column the SINFONI platescales, in which the stars have been observed, are given.

^a Definition of Silge & Gebhardt (2003)

^b Definition of Silva et al. (2008)

^c N. Neumayer, priv. comm.

**Figure 5.** a) Example fit to a 25mas spectrum and b) the according LOSVD with error bars.

scale, ten for the 100mas scale and 13 for the 250mas scale). The centres of the angular bins are at latitudes $\vartheta = 5.8^\circ$, 17.6° , 30.2° , 45.0° and 71.6° . The stellar kinematics then was extracted for all scales using the appropriate templates and α . Fig. 5 shows as an example the fit to a 25mas spectrum and the according LOSVD.

For the dynamical modelling we use these LOSVDs and no parametrized moments, but for illustration purposes we fitted the LOSVDs with Gauss–Hermite polynomials and we show the 2D fields of v , σ and the Gauss–Hermite coefficients h_3 and h_4 in Fig. 6 for all platescales. The amplitudes of the errors are on average about 8 km s^{-1} (v and σ) or 0.025 (h_3 and h_4) for the 25mas data, 4 km s^{-1} or 0.015 for the 100mas data and 9.5 km s^{-1} or 0.033 for the 250mas data.

On large scales (250mas, Fig. 6c) the galaxy is clearly rotating and the mean velocity dispersion is high ($\sigma \approx 226 \text{ km s}^{-1}$), while in the central ~ 3 arcsec (100mas, Fig. 6b) no clear rotation is visible and the dispersion is lower ($\sigma \approx 221 \text{ km s}^{-1}$). The 25mas velocity field (Fig. 6a) is irregular and with a peak in the central bins. The velocity dispersion also rises towards the centre, but the maximum does not coincide with the photometric centre. It is located $\approx 0.05 - 0.1$ arcsec south of the centre. North of the centre there is a second but less strong maximum. The two maxima are separated by a narrow, elongated σ -minimum. Outside

the central region the mean dispersion of the 25mas field is lower than in the larger fields ($\sigma \approx 218 \text{ km s}^{-1}$). h_3 and h_4 are on average small and positive.

In addition to the difficulty in explaining the structures of v and σ in the centre, it is also surprising that neither the v nor the σ peak can be seen in the 100mas data. We investigated if this is due to resolution in the following way: The 25mas data were binned 4×4 to get the same spaxel sizes as in the 100mas scale. Then the binned data were convolved with the kernel (Fig. 2c) that transforms the 25mas SINFONI image of Fornax A into the 100mas image, before being binned according to the radial and angular scheme described above. Fig. 7a shows the resulting 2D kinematic maps compared to the inner 0.8 arcsec of the 100mas data (Fig. 7b). The structures seen in the 25mas data mostly disappeared after the convolution and the convolved 25mas kinematics now look very similar to the 100mas kinematics.

The interpretation of the features seen in the unconvolved 25mas data is more difficult. In the following possible explanations are discussed.

3.4.1 Technical aspects

The features detected in the 25mas data, especially the central velocity rise, are not due to template mismatching, as they remain also when other template combinations or single templates are used. Of the nine 25mas templates, two (a K1V and a K3V star with CO EWs $\lesssim 5 \text{ \AA}$) cannot fit the data at all. With each of the other templates the kinematics of Fig. 6a can be reproduced at least qualitatively independently of the specific choice of the smoothing parameter.

The results can also be reproduced when fitting slightly different wavelength regions, as long as the CO bandheads are included. Measuring the kinematics from the other absorption lines (Ca I, Fe I and Mg I) does not work because of the weakness of the lines compared to CO. Here a much higher S/N would be required.

The central bins are very small and only cover a limited number of spaxels. Therefore one or two spaxels alone could cause the increase of v , because e.g. of an incorrect sky subtraction or bad pixel correction in the CO bandhead region of these spaxels. In addition, as the S/N of the single spaxels decreases relatively slowly from the centre to the outer parts, the S/N of the central bins is lower (~ 50) than at larger radii (60 – 80), so the errors are larger and the large velocity could be just a statistical fluctuation which would occur at larger radii as well if the S/N was equally low. A single-spaxel effect can be in principle verified or excluded by simply fitting the unbinned spectra. The problem is, that the S/N is around or below 30 which does not allow a reliable measurement of the kinematics. We first used MPL with a large α and then, as a consistency check, fitted simple Gaussians to the unbinned spectra. A central v peak is present in both cases.

3.4.2 A central disc or star cluster

Central velocity dispersion drops are common in spiral galaxies (e.g. Peletier et al. 2007) and usually associated with central discs. Central discs can be formed from gas inflow towards the centre and subsequent star formation (Wozniak et al. 2003). In early-type galaxies σ -drops are rarely

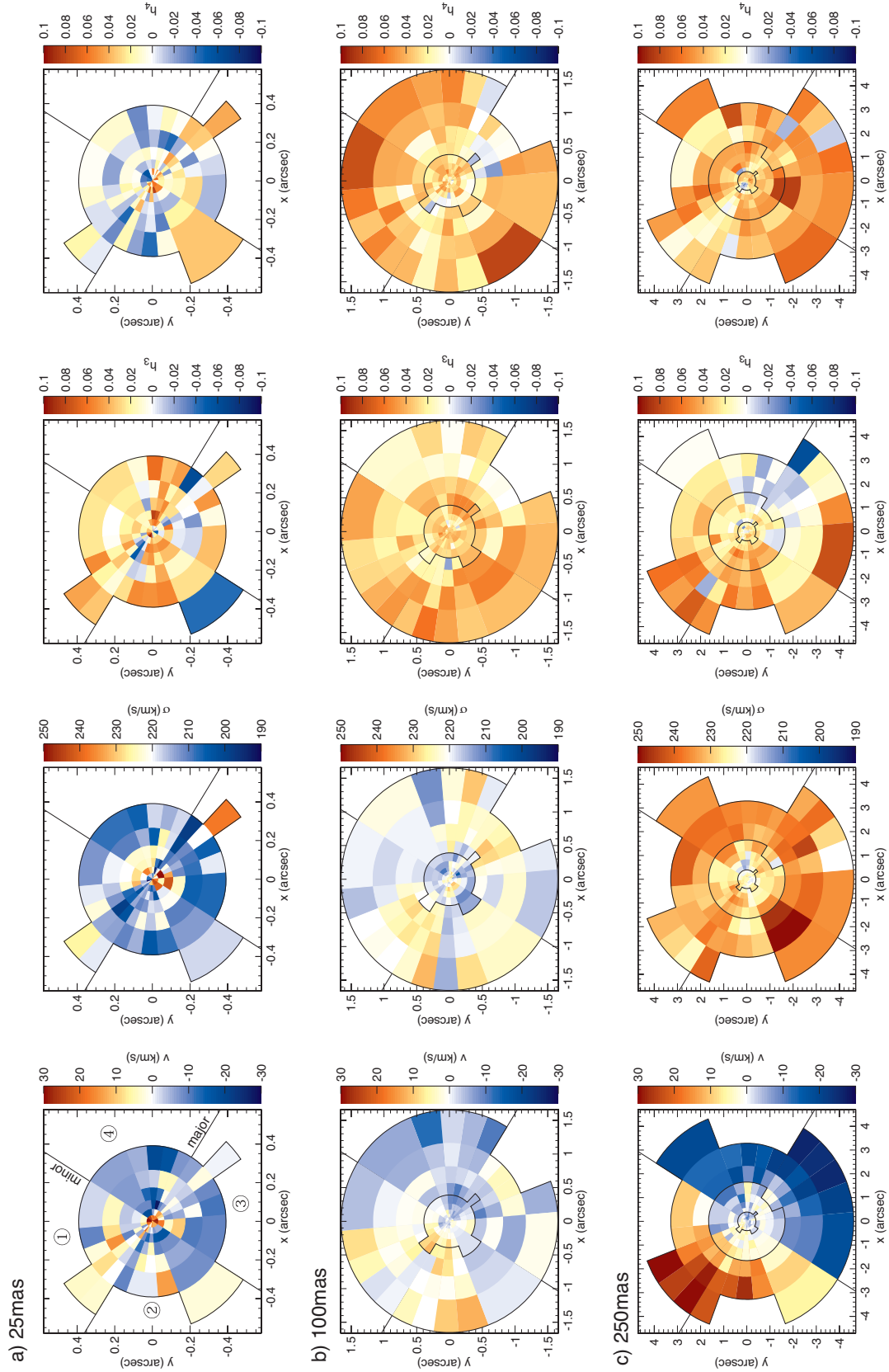


Figure 6. a) v , σ , h_3 and h_4 of Fornax A in the central 0.8 arcsec (25mas scale). The major and the minor axis as well as the numeration of the different quadrants are indicated in the velocity field (left). b) shows the same as (a) but for the 100mas scale. The 25mas field of view is marked for a better orientation. c) shows the same as (a) but for the 250mas scale. Both the 25mas and the 100mas field of view are marked.

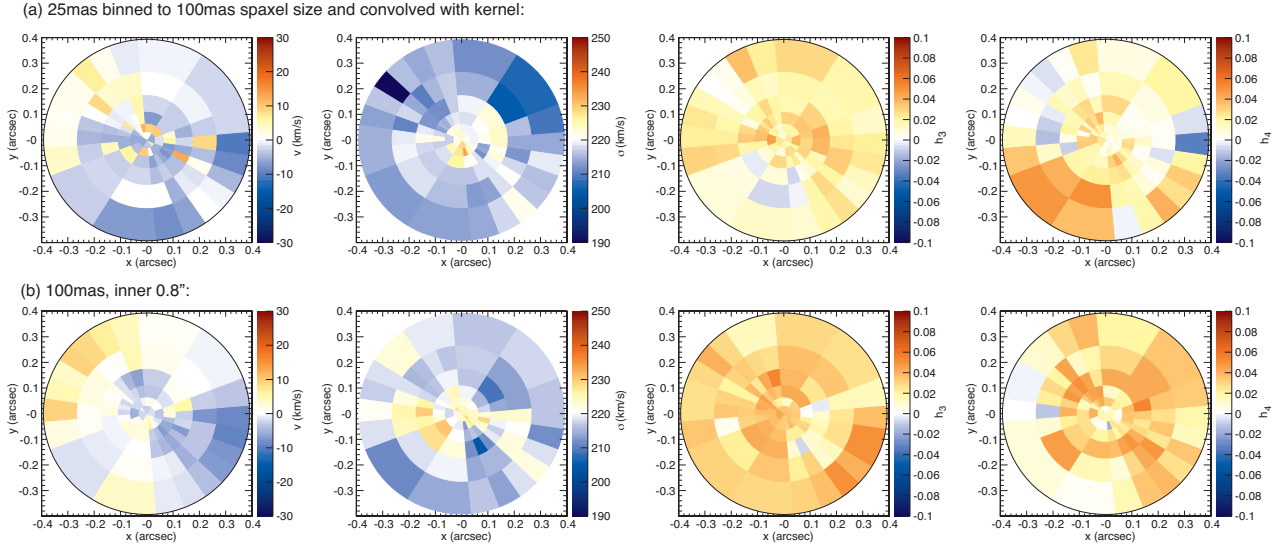


Figure 7. The 25mas data convolved with the kernel from Fig. 2c (upper row, (a)), compared to the central part of the 100mas kinematics (lower row, (b)).

found. NGC 1399 is the only case where the observed central σ -drop is discussed in detail (Houghton et al. 2006; Gebhardt et al. 2007; Lyubenova et al. 2008). Lyubenova et al. (2008) conclude that it is a dynamically distinct subsystem with a different stellar population.

Fornax A is not a clearly elliptical galaxy, but can be classified as a “peculiar” galaxy, as some remaining features like shells and ripples from a major gas-rich merger about 3 Gyr ago are still clearly visible (Schweizer 1980, 1981; Goudfrooij et al. 2001). There are also hints that a minor merger with another gas-rich galaxy happened ~ 0.5 Gyr ago (Mackie & Fabbiano 1998). Thus it would not be surprising if remainders of the merging processes were also found in the centre, like a disc produced from merger-triggered gas inflow or an infalling disc- or cluster-like central part of one of the merging components. A nuclear disc could explain the relatively thin ($\lesssim 8$ pc) and apparently elongated structure of the σ -drop. With a width of only $\lesssim 8$ pc this is probably the thinnest σ -drop ever detected. It is even narrower than the drop in NGC 1399 and also far less extended than the typical drops in spiral galaxies. As its size is comparable to the spatial resolution it is possibly unresolved. On the other hand rotation would be seen if there really was a disc.

The centre could still be unrelaxed and in the process of merging. This could induce signatures in the kinematics like those seen in Fornax A. Simulations of unequal-mass mergers with a SMBH in the primary galaxy and a significantly smaller secondary galaxy (without black hole) were performed by Holley-Bockelmann & Richstone (2000). Based on this it depends critically on the orbital decay trajectory of the secondary, and also somewhat on the black-hole mass and on the mass ratio of the galaxies, whether the secondary galaxy is destroyed by the merger or not. The time-scale for a stellar cluster falling in on a purely radial orbit – also suggested by Gebhardt et al. (2007) as one possible explanation for the σ -drop in NGC 1399 – however seems to be much shorter (of the order of about 10^7 yr) than the date of the last merger ($\sim 10^9$ yr), if the conditions in Fornax A are similar as in Holley-Bockelmann & Richstone (2000). For

nonradial mergers the formation of a rotating stellar disc is possible. As we do not know any of the details of the merger history with desirable precision for Fornax A, and as the time-scales seem to vary depending on the initial parameters of the merger simulation, it is impossible to tell whether the centre is still unrelaxed or not.

3.4.3 The effect of dust

Fornax A contains a lot of dust features (see lower panel of Fig. 3) and this dust might alter the kinematics. On the other hand observations in the K band should minimize the effects of dust and indeed already the uncorrected SOFI K_s band image shows only very little amounts of dust compared to optical HST images. Some dust is located close to the centre, but not in the central ~ 2 arcsec. Shaya et al. (1996) find a low colour excess in the central pixels of an HST WFPC $V - I$ image and conclude that here the dust extinction is only very light. Consistently the SINFONI 25mas and 100mas images also do not show any signs of dust (cf. Fig. 1). The 250mas image shows hints of dust in the SE region, spatially coincident with the high- σ region just outside the 100mas field of view. Therefore the dust outside the central 2 – 3 arcsec could be the reason for the larger average σ of the 250mas data, in agreement with the findings of Silge & Gebhardt (2003).

Due to the lack of dust in the 25mas image dust does not seem to be a plausible explanation for the central σ structure. However the scale of the effect of dust on the kinematics might depend on the location of the dust along the line of sight. E.g. a certain amount of dust directly behind the centre could have a noticeable effect without being noticed in the photometry at the given S/N. To further substantiate this we tested the effects on the kinematics when dust obscures light from stars behind or in front of the centre of a galaxy using an N-body model realisation of the best-fitting dynamical model (cf. §5.2.3) as described in Thomas et al. (2007). We calculated the kinematics of the model by

obscuring the central part at different radii and with different opacities and found that only a noticeable decrease in σ can be induced by putting a very thick layer of dust in front of the centre, but in this case the surface brightness would be reduced by more than a magnitude. Therefore we can exclude that the structure of the 25mas kinematic fields is produced by dust.

3.4.4 Stellar populations

Another explanation might be that the stellar population is different in the central region. Blue stars in the nucleus could in principle also be responsible for the low colour excess Shaya et al. (1996) find. The K band absorption line equivalent widths for Fornax A are presented in §4 in detail. The 100mas maps of the absorption line indices (Fig. 8) clearly show that the line indices change within the central ~ 0.4 arcsec. All indices show a decrease in this region, CO as the deepest absorption feature shows it most clearly. Unfortunately this trend is not as clear in the 25mas indices, as here the S/N is only about half as in the 100mas data and the scatter therefore is much larger.

Thus a dynamically colder subsystem with accordingly different line indices could be an explanation of the distorted kinematics, but the S/N of the 25mas data unfortunately is not large enough to resolve any spatial coincidence with the v peak or σ drop. Similar conclusions have been made by Lyubenova et al. (2008) for NGC 1399, where the central σ -drop coincides with a drop of the Na I and CO indices.

If a changing stellar population in the central region has an effect on the kinematics or not was tested with the N-body model mentioned in the previous section. Making the stars in the central 0.1 arcsec ten times brighter (corresponding to a ten times lower mass-to-light ratio) results only in very small changes of $\Delta\sigma = 4 \text{ km s}^{-1}$ and $\Delta h_4 = -0.002$, both within the errors of the data and much smaller than the observed variations. 100 times brighter stars would produce noticeable changes of $\Delta\sigma = 25 \text{ km s}^{-1}$ and $\Delta h_4 = -0.015$. Making the stars darker does not have an effect at all on the kinematics. As there is no photometric evidence of a very bright star cluster in the centre, we conclude that a stellar population alone, which is different from the surrounding population, is not the reason for the disturbed central kinematics.

3.4.5 AGN emission

A decrease of the line indices would also be expected for AGN, where the absorption features are diluted by the non-stellar emission of the active nucleus. In this case also the measurement of v and σ could be affected. As shown in Davies et al. (2007) the PSF can be reconstructed from the decrease of the CO equivalent width at the position of the point source. Comparing the PSF measured this way with the measured or the noisy reconstructed PSFs from Fig. 2 is difficult, because (1) we would need to measure the CO index of the unbinned spectra, which have a lower S/N than the binned ones and thus errors larger than the small $\sim 1.0 \text{ \AA}$ decrease observed in the binned spectra, and (2) for the higher S/N 100mas exposure we do not exactly know the true PSF. From the binned spectra we cannot deduce

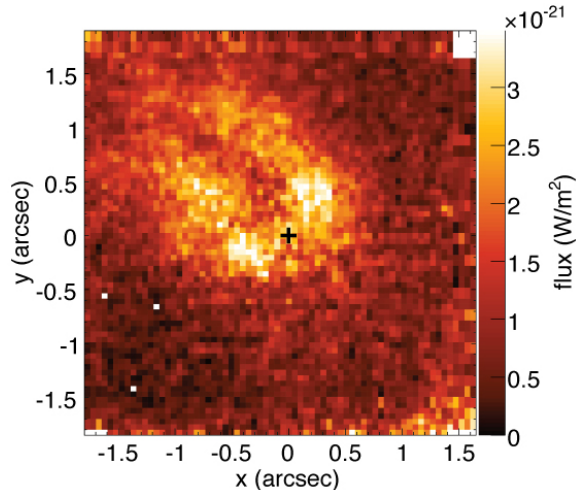


Figure 9. H₂ emission of Fornax A (100mas scale). The photometric centre is marked by a cross.

the two-dimensional PSF. A rough estimate of the FWHM of the CO dip can be obtained from fitting the averaged CO indices of a ring (red points in Fig. 8). The resulting FWHM of 0.17 arcsec in the 100mas scale is, considering the large errors introduced by the binning, well in agreement with the measured PSF. This would favour the AGN scenario.

It was found by Iyomoto et al. (1998) that the AGN in Fornax A, which powered the very luminous radio lobes, became dormant during the last 0.1 Gyr. Still the nucleus shows weak radio (Geldzahler & Fomalont 1984) and weak X-ray emission with a spectrum typical for a low-luminosity AGN (Kim & Fabbiano 2003) and is bright in the UV (Fabbiano et al. 1994). In high-S/N optical spectra several emission lines are present ([OIII], H β , NI), but very weak (Beuing et al. 2002). In the SINFONI spectra there are no apparent emission lines typical for an AGN present at the given S/N. Only weak molecular hydrogen ($1 - 0S(1) \text{ H}_2$ at $\lambda = 2.122 \text{ \mu m}$) with a S/N around 5 is found in a region north-east of the nucleus (see Fig. 9), but does not seem to be associated with the central source. The total H₂ flux in the 100mas field of view is $5.65 \times 10^{-18} \text{ W m}^{-2}$ and in a 3 arcsec aperture centred on the continuum peak it is $3.64 \times 10^{-18} \text{ W m}^{-2}$. The H₂ could be excited by X-rays, as a similar northeast-southwest elongation is present in Chandra data. This X-ray emission was associated with hot interstellar medium with a temperature of $kT = 0.62 \text{ keV}$ by Kim & Fabbiano (2003).

A weak AGN present in Fornax A would also become noticeable by a slight change of the continuum slope, making the nucleus redder. This is due to the AGN UV-continuum which heats surrounding dust that emits in the near-IR (Oliva et al. 1999). We indeed find that the slope of the continuum changes slightly in the inner ≈ 0.1 arcsec by no more than 2 – 3 per cent.

Some AGN show a certain coronal emission line in the region of the CO bandheads, which alters the measured kinematics: [Ca VIII] at 2.3213 \mu m (Portilla et al. 2008; Davies et al. 2006). As it is located directly at the left edge of the second CO bandhead, already a very small contribution can have a significant effect on the measured kinematics. We tested this using two different approaches. First we tried

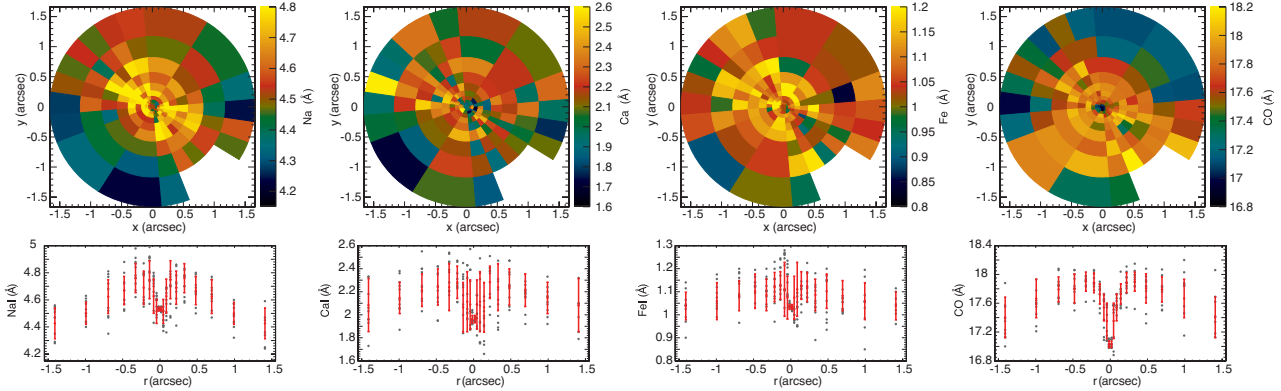


Figure 8. Na I, Ca I, $\langle \text{Fe I} \rangle$ and CO indices of Fornax A in the central 1.5 arcsec (100mas scale). The upper row shows the 2D index fields, below the position- i diagrams are shown (where i is one of the four indices). The individual values are plotted in grey, while overplotted in red are the mean indices and their rms of the bins belonging to a ring of radius r .

to measure the kinematics using only the first bandhead. The velocity map in this case has a much larger scatter and shows many peaks of 20-30 km s⁻¹ in the field of view. σ remains largely unchanged. When the first together with the third and fourth bandhead are used, the velocity map is smooth and shows no increase in the centre. The σ map is qualitatively similar to the one measured with the first two bandheads, but the absolute value of σ is much larger. The third and fourth bandheads are significantly distorted by sky emission lines and therefore do not give reliable results. The second approach was to use a standard star, convolve it with a LOSVD ($v = 0$ km s⁻¹, $\sigma = 230$ km s⁻¹, $h_3 = h_4 = 0$) and add the [Ca VIII] line with a typical FWHM of 150 km s⁻¹. The results are shown in Figs. 10 and 11. A [Ca VIII] contribution of $\lesssim 4$ per cent would not be seen in the spectra or the fit at the given S/N, but can increase v by $\lesssim 25 - 30$ km s⁻¹ and decrease σ by $\lesssim 10$ km s⁻¹ (σ measured with zero [Ca VIII] contribution is already a few km s⁻¹ lower than the real σ , see e.g. Fig. B1 in Appendix B). Therefore a weak AGN with some [Ca VIII] contribution is the most logical explanation for the observed velocity increase. The observed σ decrease probably has for the most part a different origin (most probably a stellar population effect), as it is significantly larger than the $\lesssim 10$ km s⁻¹ estimated from the simulations. In addition the high- v region only partly coincides with the low- σ region. The hint of a [Ca VIII] line signature appears when stacking all spectra within the region covered by the innermost bins and comparing it to a combination of all spectra within a ring further out ($0.11 < r < 0.17$ arcsec; see Fig. 12).

As accurate kinematics for the centre cannot be obtained from only one bandhead or by including the third and/or fourth bandhead, we will exclude the central bins in some of the dynamical models. As the black hole sphere of influence is large, this solution will not degrade the reliability of the resulting black-hole mass significantly.

4 LINE INDICES

The optical line strengths of Fornax A have been analysed extensively by Kuntschner (1998, 2000). They found a young (around 2 Gyr) and very metal-rich stellar population. The

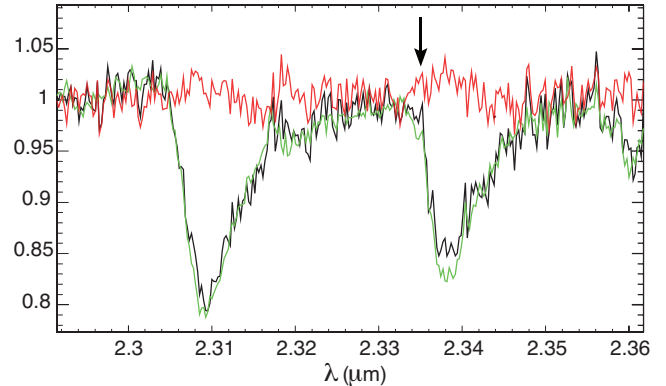


Figure 12. Combined spectra of the central region (black) at radii $r < 0.03$ arcsec and of a ring at larger radii $0.11 < r < 0.17$ arcsec (green). In red the residuals between the two spectra are plotted, shifted by +1. The position where the [Ca VIII] line is assumed to be is marked with an arrow.

optical index gradients slightly decrease with radius. Unfortunately their data have a resolution of only 1 arcsec, therefore they do not resolve the structure in the central 0.4 arcsec. The age of a number of globular clusters in Fornax A was found to be about 3 Gyr (Goudfrooij et al. 2001). Thus a plausible scenario is that the globular clusters formed during the last major merger event 3 Gyr ago (Goudfrooij et al. 2001) and that the young stellar population formed from infalling molecular gas also as a result of this merger (Horellou et al. 2001).

The spectral features in the K band can in principle be likewise interpreted in terms of age and metallicity. Unfortunately there is not such a sophisticated theoretical spectral synthesis model available yet as for optical indices and studies of K band indices are rare and often include only small samples. A recent study of Silva et al. (2008) investigates the behaviour of the K band indices of cluster stars of known age and metallicity and a sample of Fornax galaxies. Their published line indices of Fornax A are derived by extracting the mean spectrum over an aperture of 2×3 arcsec from our SINFONI 100mas data.

In Fig. 8 we show the two-dimensional K band line index maps (Na I, Ca I, $\langle \text{Fe I} \rangle$ and CO) of Fornax A for

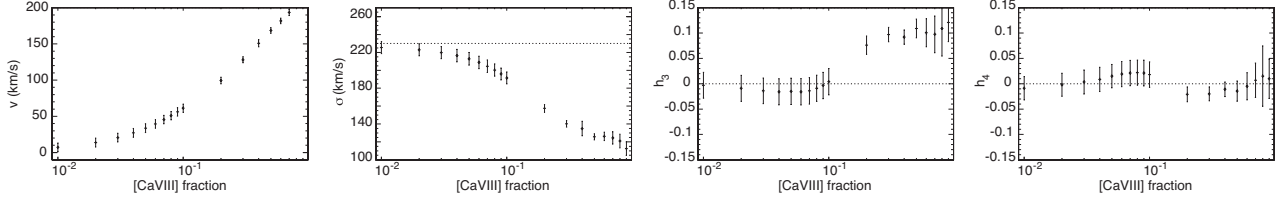


Figure 10. Mean v , σ , h_3 and h_4 as a function of [Ca VIII] contribution. The error bars are the 67 per cent intervals obtained from fitting 100 realisations of the broadened template spectrum with added noise such that the S/N is similar to the central Fornax A spectra.

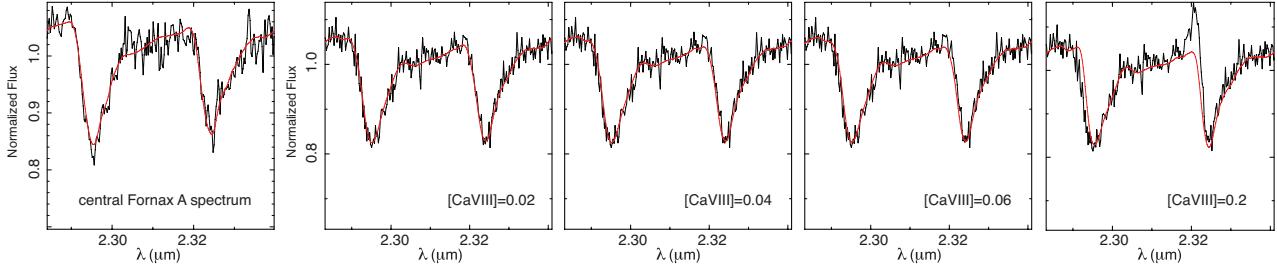


Figure 11. Fit (red) to broadened template star spectra (black) with different [Ca VIII] contributions compared to the fit to the central 25mas Fornax A spectrum with the largest measured velocity (leftmost plot).

Table 2. Mean near-IR line indices of Fornax A.

	this work	Silva et al. (2008)
Na I	4.61 (0.15)	4.70 (0.14)
Ca I	2.14 (0.21)	2.48 (0.14)
Fe I A	1.44 (0.11)	1.491 (0.066)
Fe I B	0.73 (0.09)	0.843 (0.065)
CO	17.61 (0.33)	17.53 (0.30)

Note. The indices are given in units of \AA . The middle column gives the near-IR line indices determined by averaging the values shown in Fig. 8 (upper row) and the according rms errors. The indices determined by Silva et al. (2008) are given in the right column with their errors.

the 100mas scale, because the S/N is largest for this scale. The index definitions were taken from table 6 in Silva et al. (2008). Instead of Fe I A and Fe I B we use $\langle \text{Fe I} \rangle = (\text{Fe I A} + \text{Fe I B})/2$, as they are highly correlated. The definition of the CO index is different from the definition of the CO equivalent width used above (Silge & Gebhardt 2003). Here the continuum is defined by four blue continuum bands instead of a blue and a red one. The continuum on the red side is diminished by the CO absorption bands, therefore an accurate measurement of the CO index is possible by using blue continua only. Using the definition of Silge & Gebhardt (2003) nevertheless is sufficient to decide quickly which templates to use and to notice any particularities (see Table 1 for a comparison between the CO EWs of the kinematic template stars derived by the two different index definitions). As in Silva et al. (2008) we broadened the SINFONI spectra to match the ISAAC resolution of their data and to be able to directly compare our results to their findings.

The measured indices, averaged over the entire field of view, are in good agreement with the measurements of Silva et al. (2008), as shown in Tab. 2. In two dimensions, all

indices show the same behaviour: a more or less clear dip in the centre and further out a negative gradient. This is most obvious in CO and Na I. Negative gradients are also present in the optical indices and it is therefore reasonable to assume that the K band index gradients can be likewise interpreted as age or metallicity gradients. Kuntschner (1998) find for the Fornax ellipticals that the index gradients are linked to a metallicity gradient, and not an age gradient. They assume that the negative gradients in Fornax A are likewise due to a metallicity gradient only, but their data do not go very far out in radius and therefore they cannot draw secure conclusions. Mármol-Queraltó et al. (2008) quantify a metallicity dependence of the CO index, which supports this interpretation.

What causes the dip in the very centre is less obvious. It might be one of the scenarios discussed above – AGN emission, dust or a different stellar population like a nuclear cluster or a population of younger, bluer stars of a post-starburst population. Fabbiano et al. (1994) detected a UV-bright unresolved central source with $r < 3$ pc, which according to them could be explained e.g. by a cluster of O stars or an AGN. The FWHM of the CO dip is very similar to the spatial resolution and thus unresolved, corresponding to an upper limit in size of $r \lesssim 4$ pc. Thus it is likely that the UV emission and the CO dip are caused by the same structure. Both early-type stars – due to the lack of typical late-type star absorption lines – and non-thermal emission would cause the observed decrease of all indices. Br γ absorption is the only strong feature in early-type K band stellar spectra, Br γ emission is observed in many galaxies with nuclear activity or star formation, thus this feature could be used to distinguish between these two possibilities. In the central SINFONI spectra we do not detect Br γ neither in emission nor in absorption. Thus emission or absorption is either not present, too weak to be detected, or Br γ emission and absorption just compensate. [Ca VIII] emission caused by the

AGN is also very well hidden (see Fig. 12 and discussion in §3.4.5). Due to the broader PSF its influence is eliminated in the 100mas data. Other emission lines typically present in AGN spectra are absent as well in the central region. Weak H₂ emission is present in the north-eastern region, but not correlated to the central source (see Fig. 9). In order to resolve the reasons that cause the central line index dip and kinematics, very high S/N observations with a better spatial resolution as well as self-consistent spectral synthesis models for the interpretation of the *K* band indices are needed.

5 DYNAMICAL MODELS

Based on the M_{\bullet} - σ relation of Tremaine et al. (2002) and our σ measurements a black hole with a mass around $2 \times 10^8 M_{\odot}$ would be expected. Earlier models by Shaya et al. (1996) suggest a ten times higher black-hole mass, but they rely on larger σ values. Davies (2000) observed Fornax A with the MPE 3D IFS (Weitzel et al. 1996) and measured v and σ using the CO bandheads at 2.2 μm . Their σ is lower than the values used by Shaya et al. (1996) and comparable to our values. Together with the models of Shaya et al. (1996) they obtain a SMBH mass of $\lesssim 10^9 M_{\odot}$. However, they cannot exclude that radial anisotropy may account for this large mass. A lower limit of the central mass concentration of 75 M_{\odot} was estimated by Fabbiano et al. (1994) based on the measured nuclear UV emission.

We used the axisymmetric code of Gebhardt et al. (2000a, 2003) in the version of Thomas et al. (2004) to determine the mass of the SMBH in Fornax A. It is based on the Schwarzschild (1979) orbit superposition technique and comprises following steps: (1) Calculation of the gravitational potential of the galaxy from the stellar mass density ρ_{\star} using a trial black-hole mass M_{\bullet} and mass-to-light ratio Υ . (2) Generation of an orbit library for this potential and construction of a weighted superposition of orbits that best matches the observational constraints. (3) Repetition of the first two steps with different values for Υ and M_{\bullet} until the eligible parameter space is systematically sampled. The best-fitting parameters then follow from a χ^2 -analysis. Our orbit libraries contain around 2×7000 orbits. The de-projected luminosity density is a boundary condition and hence exactly reproduced, while the LOSVDs are fitted in 25 velocity bins between $-880 \dots +880 \text{ km s}^{-1}$ with a bin width of $\approx 75 \text{ km s}^{-1}$. Special care was taken when implementing the PSF. Due to its asymmetric shape the PSF was not fitted, but the models were rather convolved with the two-dimensional image of the PSF reference star directly (cf. Nowak et al. 2007). All modelling was done with minimal regularisation.

A big advantage of integral-field data compared to longslit data only is the assurance of whether the assumption of axisymmetry is legitimate by comparing both the kinematics and the results of the dynamical modelling of all four quadrants. In case all quadrants produce the same results, the data can be folded and averaged, so that the errors are reduced. This results in a very large number of models. For Fornax A we calculated around 5000 models in total, covering a broad parameter space in M_{\bullet} ($0 \dots 5 \times 10^8 M_{\odot}$) and Υ (0.55 \dots 0.95) for each quadrant, several combinations of datasets and PSFs using an inclination of 90° . At the begin-

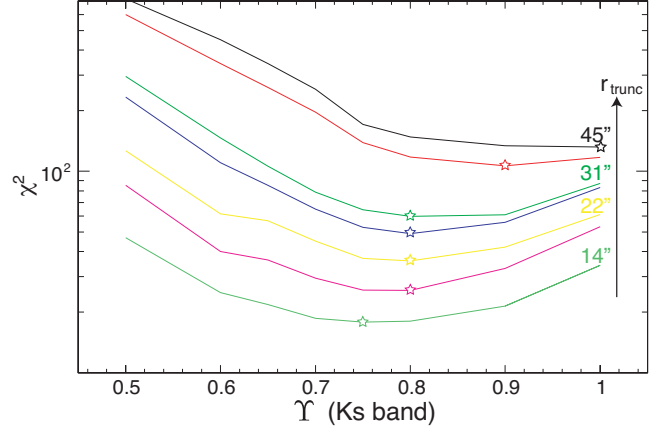


Figure 13. χ^2 as a function of mass-to-light ratio Υ for models calculated with the longslit data alone, truncated at different radii r_{trunc} and without black hole. The models with the smallest χ^2 are marked with a star.

ning we computed some test models using either the longslit data only (§5.1.1) or the SINFONI data only (§5.1.2) in order to constrain the Υ range. As a second step each of the four quadrants was modelled separately using the longslit data and either the 25mas data (§5.2.1) or the 100mas data (§5.2.2) or a combination of the two (§5.2.3). This step is essential as it reveals possible inconsistencies between the datasets, non-axisymmetries and other problems. The assumed diameter of the sphere of influence is around 0.46 arcsec, resolved by both SINFONI datasets. The 250mas data were not included in the modelling, as they do neither resolve the sphere of influence nor do they add significantly more information in the outer parts that would justify the enhanced amount of computing time. After a careful examination of the results and verifying the consistency of the data with axisymmetry, the four quadrants were averaged and modelled for the same combination of datasets as for the single quadrants.

5.1 The stellar dynamical *Ks* band mass-to-light ratio Υ

In order to check if the stellar mass-to-light ratios Υ obtained for individual datasets, agree and if they are consistent with Υ from population synthesis models (Maraston 1998, 2005), we determine Υ by modelling single datasets.

5.1.1 Υ from longslit data

First a number of models were calculated using exclusively the longslit data without black hole covering a broad range in Υ (in units of M_{\odot}/L_{\odot}^{Ks}). The longslit data were truncated at different radii r_{trunc} between 14 arcsec and 45 arcsec. The resulting best-fitting Υ (Fig. 13) is roughly constant with r_{trunc} and ≈ 0.75 – 0.8 for longslit data at $r_{\text{trunc}} \lesssim 31 \text{ arcsec} \approx 2.8 \text{ kpc}$, which roughly corresponds to the effective radius of Fornax A ($R_e = 36_{-11.2}^{+5.7} \text{ arcsec}$, Bedregal et al. 2006). At larger truncation radii Υ increases strongly, a sign that here the dark halo starts to have an effect. This is consistent with the results of Thomas et al. (2007), who found dark matter fractions of ≈ 30 per cent at 3 kpc in similar bright

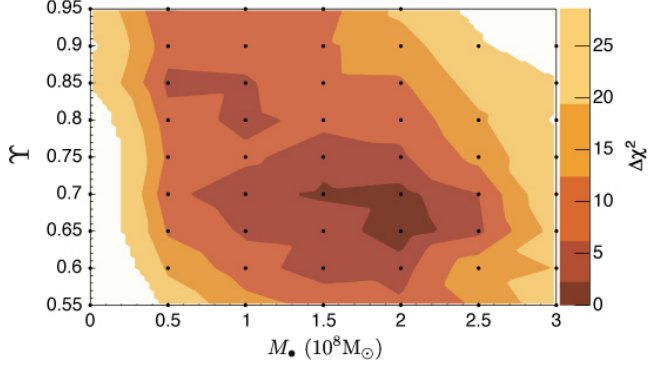


Figure 14. $\Delta\chi_0^2 = \chi^2 - \chi_{\min}^2$ as a function of Υ (Ks band) for models calculated with the SINFONI 100mas data alone and a small number of black-hole masses M_\bullet . The coloured regions are the $1 \dots 5\sigma$ errors in $\Delta\chi_0^2$. Each black dot represents a model.

Coma galaxies. Thus in the following only longslit data at $r < 31$ arcsec will be used for the dynamical modelling.

5.1.2 Υ from SINFONI data

For the SINFONI 100mas data alone the best-fitting Υ is slightly lower (≈ 0.7 in units of M_\odot/L_\odot^{Ks} , see Fig. 14), but within the errors consistent with Υ derived from the longslit data alone. The contours are strongly elongated towards large Υ with slightly decreasing M_\bullet , as large Υ in the centre can somewhat compensate a lower M_\bullet . This degeneracy between M_\bullet and Υ is even stronger for the tiny field of view 25mas data alone, where Υ cannot be constrained very well. This emphasizes the importance of including the longslit data in the dynamical modelling, which makes the degeneracy virtually disappear.

In order to be able to compare our stellar dynamical Ks band Υ to predictions from population synthesis models, we need to scale it to units of M_\odot/L_\odot^K by multiplying it with the ratio of the bandwidths:

$$\Upsilon_K = \Upsilon \frac{\Delta Ks}{\Delta K} = \Upsilon \frac{0.275 \mu\text{m}}{0.390 \mu\text{m}} \approx 0.5$$

For a 2 – 3 Gyr old population with a high metallicity [Z/H] = 0.3 – 0.45 (Kuntschner 1998, 2000) the models of Maraston (1998, 2005) predict $\Upsilon_K \approx 0.3 \dots 0.6$ (Salpeter IMF) and $\Upsilon_K \approx 0.2 \dots 0.4$ (Kroupa IMF). Thus the measured stellar dynamical Υ is in good agreement with a Salpeter IMF but larger than predicted for a Kroupa IMF. When taking into account the error in the measured dynamical Υ and a possible error in the distance assumed for Fornax A, then the dynamical Υ is marginally in agreement also with the Kroupa IMF. Cappellari et al. (2006) also find that the dynamical Υ for E/S0 galaxies are in agreement or larger than the Υ predicted using a Kroupa IMF.

5.2 The black-hole mass M_\bullet

5.2.1 M_\bullet from the 25mas and the longslit data

After having constrained the possible Υ range we now focus on the determination of the mass of the central black hole. We modelled the 25mas dataset together with the

longslit data for each quadrant separately and at an inclination of 90° . The resulting values for M_\bullet and Υ with the 3σ error bars are listed in Tab. 3. The best-fitting black-hole masses and mass-to-light ratios are in the range $M_\bullet = (2.0 \dots 3.25) \times 10^8 M_\odot$ and $\Upsilon = 0.675 \dots 0.775$ and agree very well within 2σ ($\Delta\chi_0^2 = \chi^2 - \chi_{\min}^2 = 6.2$) errors.

5.2.2 M_\bullet from the 100mas and the longslit data

The same was done using only the 100mas dataset together with the longslit data and the measured PSF. Both M_\bullet and Υ are in agreement between the different quadrants, but slightly smaller than for the 25mas data ($M_\bullet = 1.0 \dots 2.0 \times 10^8 M_\odot$, $\Upsilon = 0.65 \dots 0.7$). Within $2 - 3\sigma$ errors they still agree with the 25mas results. Note that the sphere of influence is well resolved in both cases.

To figure out whether the uncertainties in the PSF could raise a bias in M_\bullet , the same models were calculated with the 25mas PSF convolved with the kernel from Fig. 2c. The results are virtually identical (see Tab. 3). Therefore, slight uncertainties in the PSF shape do not have a noticeable effect on M_\bullet or Υ .

As a cross-check the 25mas data, binned 4×4 to achieve the 100mas spaxel size and convolved with the kernel, were also modelled using the convolved 25mas PSF. In this case the confidence intervals are much wider and the best-fitting values agree within $1 - 2\sigma$ with both the 25mas and the 100mas results.

The difference between the two scales could be related to the different spatial coverage, although in that case we would expect a similar result with larger error bars for the 25mas models. An increase of Υ towards the centre could also be an explanation. The global Υ would basically not change in that case, and a larger black-hole mass could mimic the Υ gradient. A triaxial structure could also cause a systematic difference between the 25mas and the 100mas scale.

Due to the good overall agreement of the different quadrants this implies that the assumption of axisymmetry is justified and therefore the four quadrants of each dataset were folded and averaged. The results of the averaged data agree with the results of the individual quadrants.

5.2.3 M_\bullet from the longslit and a combination of the 25mas and the 100mas data

In order to take advantage of the high spatial resolution of the 25mas dataset and to constrain the orbital distribution of the galaxy adequately the 25mas data were combined with the 100mas data and this combined dataset was modelled together with the longslit data. The spatial region covered already by the 25mas data was not considered in the 100mas dataset. The results of the dynamical modelling are shown in Tab. 3 and Fig. 15, where $\Delta\chi_0^2$ is plotted as a function of M_\bullet and Υ with error contours for two degrees of freedom. All four quadrants deliver the same results within at most 3σ errors when all data bins are considered (the mean black-hole mass is $\langle M_\bullet \rangle = 1.3 \times 10^8 M_\odot$ with a corresponding $\text{rms}(M_\bullet) = 0.4 \times 10^8 M_\odot$ and the mean Ks band mass-to-light ratio is $\langle \Upsilon \rangle = 0.68$ with a corresponding $\text{rms}(\Upsilon) = 0.03$). When the inner two radial bins are excluded the results are almost identical ($\langle M_\bullet \rangle = 1.2 \times 10^8 M_\odot$,

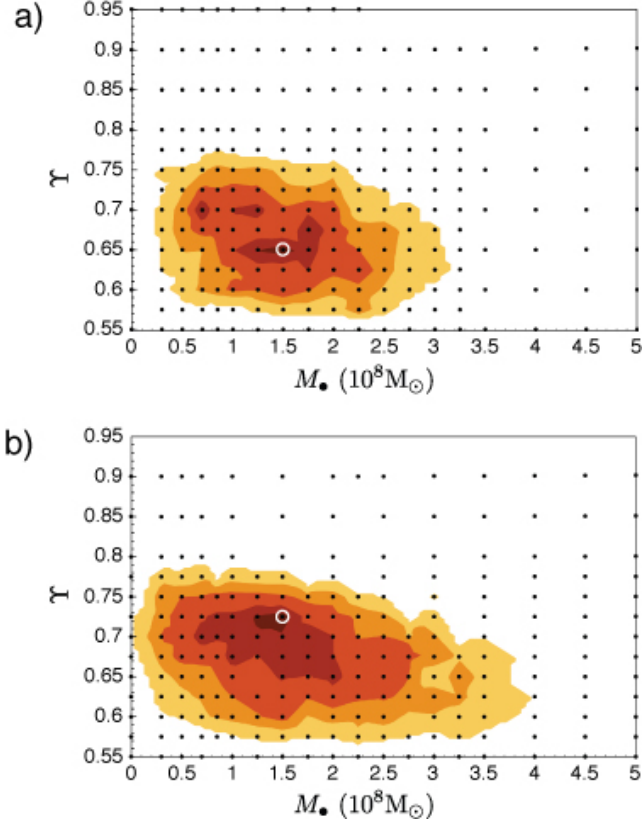


Figure 16. Same as Fig. 15 (longslit, 100mas and 25mas data) but for the averaged quadrant with (a) or without (b) the bins of the central two radii.

$\text{rms}(M_{\bullet}) = 0.5 \times 10^8 M_{\odot}$, $\langle \Upsilon \rangle = 0.70$ and $\text{rms}(\Upsilon) = 0.02$). Only the individual $\Delta\chi^2_0$ contours are wider because of the decreased resolution in the centre.

As the single quadrants agree well with each other it is legitimate to just model the LOSVDs folded and averaged over all quadrants. This is shown in Fig. 16 for both the entire dataset (Fig. 16a) and with the central bins excluded (Fig. 16b). After the averaging the central velocity peak disappears, as the LOSVDs of the third and fourth quadrant are mirrored. The results therefore are in both cases very similar. They also agree very well with the single quadrants. The black hole mass of Fornax A, derived from modelling the averaged LOSVDs of the combined 25mas and 100mas SINFONI dataset and longslit data, is $M_{\bullet} = 1.5^{+0.75}_{-0.8} \times 10^8 M_{\odot}$ and the according mass-to-light ratio is $\Upsilon = 0.65^{+0.075}_{-0.05}$ (3σ errors). The fit of the best-fitting model to v , σ , h_3 and h_4 along the major and the minor axis is shown in Fig. 17. Note that the best fit without black hole would be hardly distinguishable from the shown fit with black hole (see discussion below and Fig. 18). The result does not change when the inner two radial bins, where the AGN emission distorts the CO absorption bands are excluded. Only the error bars become somewhat larger ($M_{\bullet} = 1.5^{+1.25}_{-1.2} \times 10^8 M_{\odot}$ and $\Upsilon = 0.725^{+0.025}_{-0.125}$). Note that the 1σ errors derived from a smoothed version of the χ^2 profile agree well with the rms of the four quadrant's solution (see above).

In order to illustrate the significance of the result and where the influence of the black hole is largest, Fig. 18 shows the χ^2 differences between the best-fitting model without

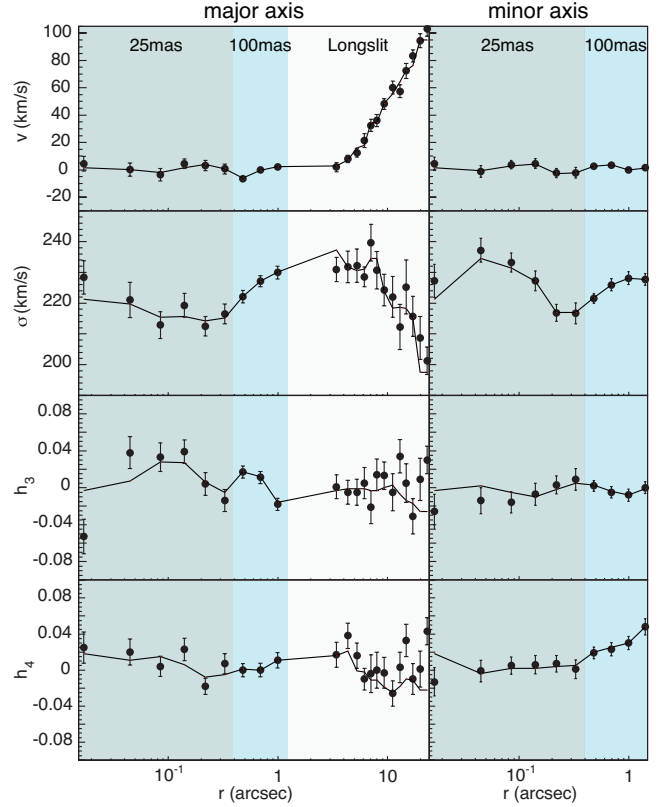


Figure 17. Fit (solid line) of the best model with $M_{\bullet} = 1.5 \times 10^8 M_{\odot}$ and $\Upsilon = 0.65$ to the major and minor axis kinematics (points).

black hole and the best-fitting model with black hole for all LOSVDs of the averaged quadrant, analogous to fig. 7 in (Nowak et al. 2007). As in the case of NGC 4486a the largest black hole signature is found within about 2 spheres of influence and in particular along the major axis. For about 85 per cent of all bins the model with black hole produces a fit to the LOSVD better than the model without black hole. Adding a black hole improves the fit everywhere and not only in the centre, because orbit-based models have a lot of freedom and will choose a different orbit distribution if no black hole is assumed. Or put in another way: a model without a black hole will not just be worse in the very centre but will be worse over a relatively large area of the galaxy. For the bins with the largest $\Delta\chi^2$ along the major axis the LOSVD and the fits with and without black hole are shown in the left part of Fig. 18 together with the corresponding $\Delta\chi^2_i$ as a function of line-of-sight velocity. The largest χ^2 differences appear in the high-velocity tails of the LOSVDs. The total χ^2 difference, summed over all LOSVDs, between the best model with black hole and the best model without black hole is $\Delta\chi^2 = 54.7$, which corresponds to about 7.1σ . The total χ^2 values for the models are around 450. Together with the number of observables (60 LOSVD bins \times 25 velocity bins) this gives a reduced χ^2 of ≈ 0.3 . This is a reasonable value as the effective number of observables is smaller due to the smoothing (Gebhardt et al. 2000a).

For the best-fitting model ($\Upsilon = 0.65$) the total stellar mass within 1 sphere of influence, where the imprint of the black hole is strongest, is $M_{*} = 1.11 \times 10^8 M_{\odot}$. If

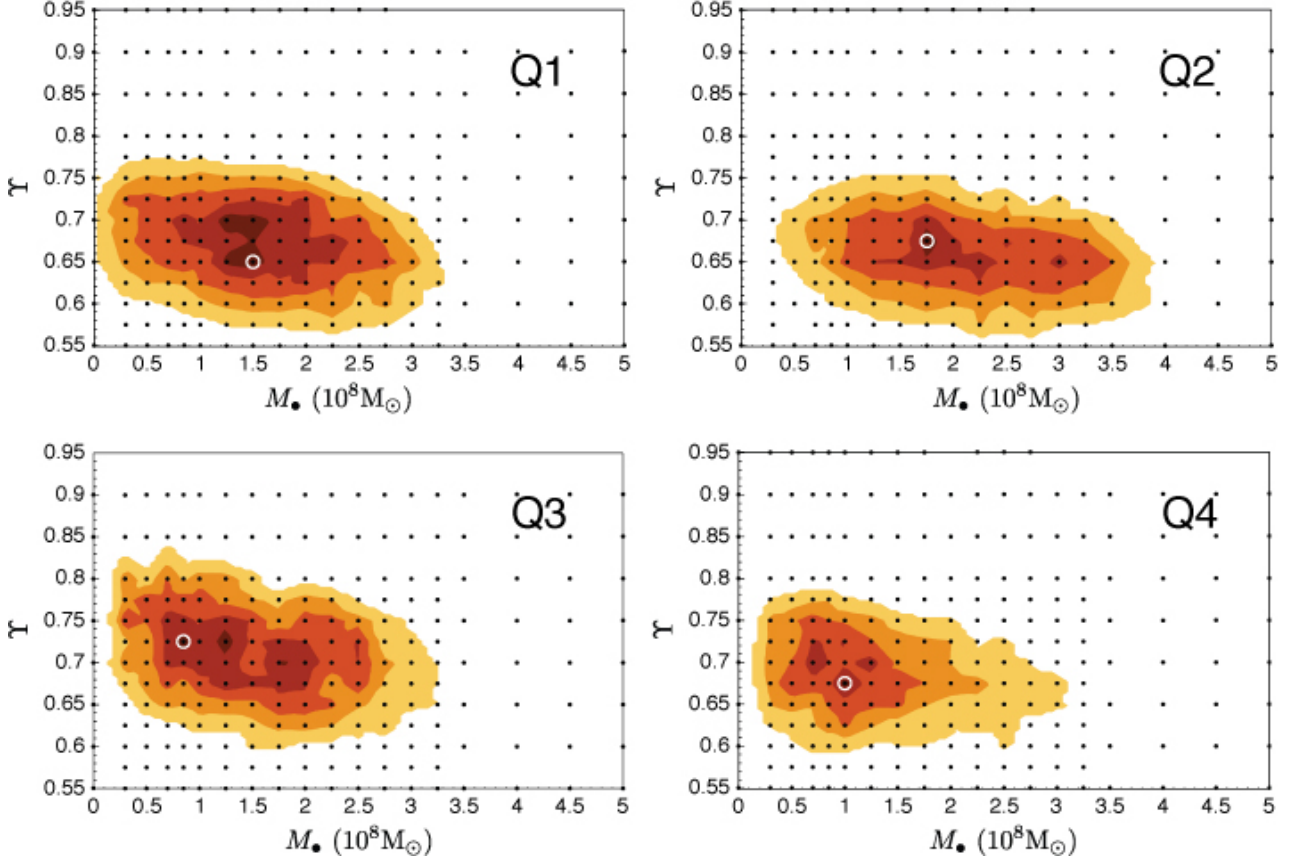


Figure 15. Models calculated for all four quadrants using a combination of longslit data out to 31 arcsec, 100mas and 25mas SINFONI data. For each quadrant $\Delta\chi_0^2 = \chi^2 - \chi_{\min}^2$ is plotted as a function of the black-hole mass M_\bullet and the Ks band mass-to-light ratio Υ . The coloured regions are the 1...5 σ confidence intervals for two degrees of freedom ($\Delta\chi_0^2 = 2.28, 6.20, 12.43, 19.44$ and 28.65). Each model that was calculated is marked as a black dot, the best-fitting model is encircled by a white ring. The $\Delta\chi_0^2$ contours are unsmoothed, which sometimes results in disconnected 1 σ regions due to noise in the models (e.g. in Q3).

the additional mass of $M_\bullet = 1.5 \times 10^8 M_\odot$ was entirely composed of stars, the mass-to-light ratio would increase to $\Upsilon = 1.53$ (corresponding to $\Upsilon_K = 1.08$). This value would be typical for an old stellar population (around 8 Gyr for a Salpeter IMF, or 13 Gyr for a Kroupa IMF), which has not been found in Fornax A (Goudfrooij et al. 2001; Kuntschner 2000).

Fig. 19 shows the anisotropy profiles for the best-fitting model with black hole and the best-fitting model without black hole. The models with black hole become tangentially anisotropic in the centre ($r \lesssim 0.2$ arcsec), while the models without black hole show a certain degree of radial anisotropy ($\sigma_r/\sigma_t \approx 1.3$ where $\sigma_t = [(\sigma_\theta^2 + \sigma_\phi^2)/2]^{1/2}$). This behaviour is not surprising, as a central velocity dispersion increase can be modelled with either a large black-hole mass or with radial orbits. However, the no black hole case is a significantly poorer fit than the best-fitting case with black hole. At large radii the tangential bias is decreased with an increasing black-hole mass, but the anisotropy profile in this region is difficult to interpret since we did not include a dark halo.

6 SUMMARY & DISCUSSION

We have obtained near-IR integral field data with three different spatial resolutions ≥ 0.085 arcsec for the merger remnant Fornax A. Stellar rotation is only detected in the outer parts ($r \gtrsim 1.5$ arcsec). The stellar velocity dispersion slightly decreases from large to smaller radii. In the highest resolution data it shows two peaks in the centre, separated by a narrow low- σ region. The average dispersions are $\sigma = 226 \pm 9$ km s $^{-1}$ in an 8 arcsec diameter aperture, $\sigma = 221 \pm 4$ km s $^{-1}$ in a 3.0 arcsec diameter aperture and $\sigma = 218 \pm 8$ km s $^{-1}$ in an 0.8 arcsec diameter aperture. A low-luminosity AGN is likely to be present and distort the stellar kinematics in the central $\lesssim 0.06$ arcsec, where weak [Ca VIII] emission in the region of the second CO band-head probably induces a velocity peak. The σ -drop can be at most partially attributed to this emission line. Either the AGN continuum emission or a cold stellar subsystem or both could be the cause.

Near-IR line indices were measured using the high-S/N, intermediate resolution data to trace stellar populations. All indices show the same trend, a negative gradient and in the centre an unresolved depression. The negative gradient of the CO index can be interpreted as a metallicity gradient. The central drop ($\sim 1\text{\AA}$ in CO) could be, like the σ drop,

Table 3. Resulting black-hole masses M_{\bullet} and Ks band mass-to-light ratios Υ with the according 3σ ($\Delta\chi_0^2 = 12.43$) errors for all modelled datasets and quadrants.

Dataset	Quadrant	M_{\bullet} [$10^8 M_{\odot}$]	$M_{\bullet,-}^a$	$M_{\bullet,+}^b$	Υ	Υ_-^c	Υ_+^d
25mas ^e +LS ^f	1	2.0	0.3	3.5	0.725	0.625	0.775
	2	3.25	1.5	4.0	0.675	0.625	0.75
	3	2.5	0.7	3.25	0.75	0.675	0.825
	4	2.0	0.3	4.0	0.775	0.675	0.825
	1–4 a ^g	1.75	0.7	3.0	0.7	0.625	0.75
	1–4 a c ^h	3.0	0.3	4.5	0.7	0.65	0.75
100mas ⁱ +LS	1	1.5	0.7	2.5	0.65	0.625	0.7
	2	1.25	0.85	2.75	0.7	0.6	0.7
	3	1.0	0.3	2.0	0.675	0.65	0.75
	4	2.0	0.5	3.0	0.675	0.625	0.725
	1–4 a	1.0	0.3	1.75	0.65	0.6	0.725
100mas conv. ^j +LS	1	1.5	0.5	2.0	0.65	0.65	0.7
	2	1.5	0.7	2.5	0.7	0.65	0.7
	3	1.0	0.3	1.5	0.7	0.65	0.75
	4	2.0	0.5	2.5	0.7	0.65	0.7
25mas conv. ^k +LS	1	2.0	0.0	4.0	0.7	0.65	0.8
	2	1.5	0.3	4.0	0.7	0.65	0.8
	3	0.7	0.3	3.5	0.8	0.7	0.85
	4	1.0	0.3	2.5	0.75	0.7	0.8
25mas+100mas+LS	1	1.5	0.3	2.75	0.65	0.625	0.725
	2	1.75	1.0	3.5	0.675	0.625	0.7
	3	0.85	0.3	2.5	0.725	0.65	0.8
	4	1.0	0.5	1.75	0.675	0.625	0.75
	1–4 a	1.5	0.7	2.25	0.65	0.6	0.725
	1 c	1.5	0.3	3.0	0.7	0.625	0.75
	2 c	1.75	0.5	3.0	0.675	0.625	0.725
	3 c	0.85	0.3	2.5	0.725	0.675	0.8
	4 c	0.7	0.3	2.0	0.7	0.65	0.75
	1–4 a c	1.5	0.3	2.75	0.725	0.6	0.75

Note. When only one SINFONI dataset was included in the modelling, the M_{\bullet} - Υ parameter space was sampled more coarsely than for the combined SINFONI dataset, with only about half the number of models per quadrant. This can sometimes result in the lower or upper limits being identical to the best-fitting values.

^a Lower 3σ limit of M_{\bullet} [$10^8 M_{\odot}$]

^b Upper 3σ limit of M_{\bullet} [$10^8 M_{\odot}$]

^c Lower 3σ limit of Υ

^d Upper 3σ limit of Υ

^e SINFONI data with a field of view of 0.8×0.8 arcsec

^f Longslit data from the Siding Spring 2.3m telescope (Saglia et al. 2002)

^g The LOSVDs of all four quadrants were averaged and then modelled

^h Central two radial bins excluded due to AGN contamination

ⁱ SINFONI data with a field of view of 3.0×3.0 arcsec together with the measured PSF were modelled

^j 100mas SINFONI data were modelled together with the PSF from Fig. 2d

^k 25mas SINFONI data, binned to the 100mas spaxel scale. Data and PSF were then convolved with the kernel from Fig. 2c

caused by the low-luminosity AGN, a subsystem with a different stellar population, or a combination of the two.

Using an axisymmetric Schwarzschild code we find a black hole with the mass $M_{\bullet} = 1.5_{-0.8}^{+0.75} \times 10^8 M_{\odot}$ (3σ C.L. for two degrees of freedom), when the 25mas, the 100mas and the longslit data are included. The same mass with

slightly larger error bars is found when the innermost bins, where the kinematics is distorted by the AGN, are excluded from the dynamical modelling. The assumption of axisymmetry is justified as consistent results were obtained when modelling single quadrants. The mean black-hole mass obtained from the four single quadrants is $\langle M_{\bullet} \rangle = 1.3 \times 10^8 M_{\odot}$

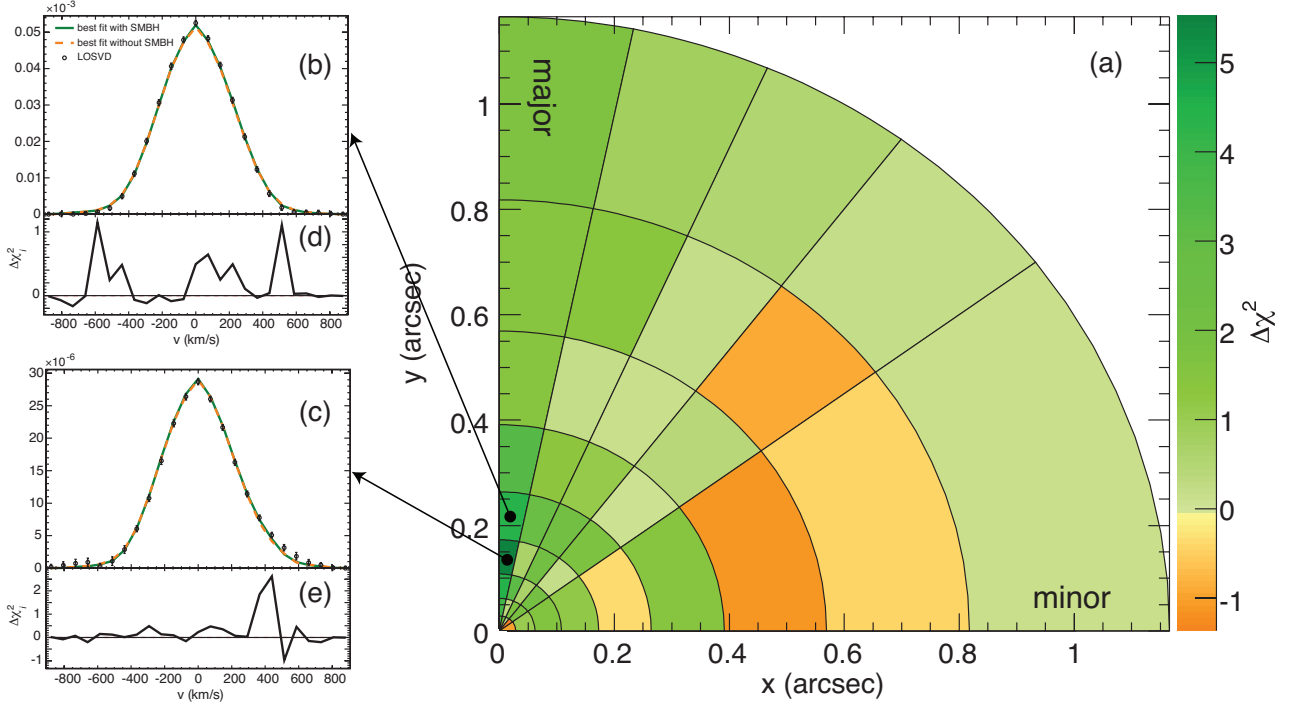


Figure 18. (a) χ^2 difference between the best-fitting model without black hole and the best-fitting model with black hole ($\Delta\chi^2 = \sum_i \Delta\chi_i^2 = \sum_{i=1}^{25} (\chi_{i,\text{noBH}}^2 - \chi_{i,\text{BH}}^2)$) over all 25 velocity bins for all LOSVDs of the averaged quadrant (longslit, 100mas and all 25mas SINFONI data). Bins where the model with black hole fits the LOSVD better are plotted in green the others in orange. (b,c) For the radii with the largest positive χ^2 difference in (a) the LOSVD (open circles with error bars, normalised as in Gebhardt et al. (2000a)) and both fits (with black hole, full green line, and without black hole, dashed orange line) are shown with the corresponding $\Delta\chi_i^2$ plotted below (d,e).

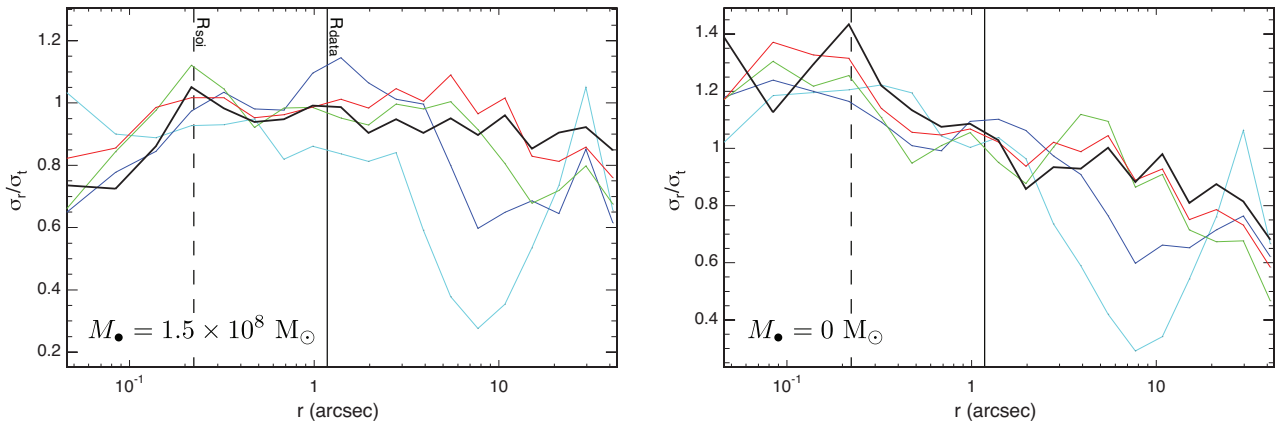


Figure 19. Radial over tangential anisotropy as a function of radius for the best-fitting model with black hole (left) and the best-fitting model without black hole (right). The values along the major axis are plotted in black, those along the minor axis in cyan and the other colours represent the position angles in between. The vertical dashed line indicates the radius of the sphere of influence and the vertical solid line marks the radius out to which the SINFONI data used in the models extend.

with $\text{rms}(M_\bullet) = 0.4 \times 10^8 M_\odot$ and the mean K s band mass-to-light ratio is $\langle \Upsilon \rangle = 0.68$ with $\text{rms}(\Upsilon) = 0.03$, in agreement with the 1σ limit derived from the analysis of the smoothed χ^2 -profile for the averaged data. The PSF of the 100mas data could not be measured very accurately, but this does not seem to have noticeable effects. Modelling the 100mas data with the measured or a reconstructed, noisier PSF (both have about the same FWHM) does not yield different results.

We find a dynamical K s band mass-to-light ratio of $\Upsilon = 0.65_{-0.05}^{+0.075}$. When the inner two radial bins are not included it is somewhat larger ($\Upsilon = 0.725_{-0.125}^{+0.025}$). This is in agreement with stellar population models assuming a Salpeter IMF, but only marginally consistent with a Kroupa IMF. A dark halo plays a significant role only outside ~ 31 arcsec, close to the effective radius ($R_e = 36$ arcsec, Bedregal et al. 2006). We therefore included neither a dark halo nor longslit data at radii larger than 31 arcsec.

The black-hole mass expected from the M_{\bullet} - σ relation (Tremaine et al. 2002) is $(2.2 \pm 0.4) \times 10^8 M_{\odot}$. Note that estimating σ_e , the luminosity-weighted velocity dispersion within R_e , from Fig. 17 gives the same value as σ measured in the 8 arcsec aperture quoted above. This mass is consistent with our measurements within the errors. Fornax A is only one of two galaxies that underwent a major merger a few Gyr ago where a black-hole mass has been measured (the other one is Cen A, e.g. Neumayer et al. 2007). Both seem to be consistent with the M_{\bullet} - σ relation, which holds important implications for the growth of the black hole and its surrounding bulge. Despite still showing obvious characteristics of the merging process – like shells and ripples in the outer envelope and disordered dust features throughout the entire galaxy – the black hole of Fornax A has about the mass expected for a normal elliptical. This suggests that bulges and black holes grow approximately synchronously in the course of a merger, or that the growth is regulated during the active phase.

The black-hole mass of Fornax A is, however, not in agreement with the relations between black-hole mass and K band luminosity L_K or bulge mass M_{bulge} of Marconi & Hunt (2003). The total 2MASS K_s band magnitude $m_{K_s} = 5.587$ corresponds to $\log(M_{\text{bulge}}/M_{\odot}) \approx 11.4$ for our $\Upsilon_{K_s} = 0.65$. For this high bulge mass a black-hole mass of $\sim 6 \times 10^8 M_{\odot}$ would be expected, a factor ~ 4 larger than what we measured. Interestingly the situation is similar for Cen A. With the K band magnitude given in Marconi & Hunt (2003) and $\Upsilon_K=0.72$ (Silge et al. 2005) the bulge mass is $\log(M_{\text{bulge}}/M_{\odot}) \approx 11.0$ and a black hole with $M_{\bullet} \approx 2.2 \times 10^8 M_{\odot}$ would thus be expected, a factor ~ 5 larger than the mass of $4.5 \times 10^7 M_{\odot}$ obtained by Neumayer et al. (2007). In this context it would be interesting to reconsider the relationship between $M_{\bullet}/M_{\text{bulge}}$ and galaxy age found by Merrifield et al. (2000). Fornax A and Cen A both have a very small $M_{\bullet}/M_{\text{bulge}}$ and they would be among the youngest galaxies in their sample. Although the number of merger galaxies with measured black-hole masses is fairly small, a correlation between the time of the last major merger and M_{\bullet} might start to emerge.

In order to draw more stringent conclusions on the connections between merging, bulge growth, black hole growth and nuclear activity more dynamical black-hole mass measurements in merger remnants and in luminous AGN are necessary. We were able to show that reliable black hole masses can be derived via stellar dynamical modelling even if the nuclear source makes dynamical measurements in the centre impossible, as long as the spatial resolution is high enough that the AGN signature is well within the sphere of influence.

ACKNOWLEDGMENTS

We would like to thank the Paranal Observatory Team for support during the observations. We are very grateful to Harald Kuntschner for providing us the code to measure near-IR line indices, to Mariya Lyubenova for helping us implementing the software and numerous discussions about line indices, and to Yuri Beletsky for providing us the SOFI images of Fornax A. Furthermore we thank Peter Erwin and Robert Wagner for stimulating discussions. Finally we thank

the referee for his useful comments. This work was supported by the Cluster of Excellence: “Origin and Structure of the Universe” and by the Priority Programme 1177 of the Deutsche Forschungsgemeinschaft.

REFERENCES

- Abuter R., Schreiber J., Eisenhauer F., Ott T., Horrobin M., Gillessen S., 2006, *New Astronomy Review*, 50, 398
- Arnaboldi M., Freeman K. C., Gerhard O., Matthias M., Kudritzki R. P., Méndez R. H., Capaccioli M., Ford H., 1998, *ApJ*, 507, 759
- Bedregal A. G., Aragón-Salamanca A., Merrifield M. R., Milvang-Jensen B., 2006, *MNRAS*, 371, 1912
- Beletsky Y., Moiseev A., Alves J., Kniazev A., 2008, The inner structure of the merger galaxy NGC 1316 (Fornax A): a normal boxy elliptical with a kinematically decoupled core, submitted
- Bender R., Moellenhoff C., 1987, *A&A*, 177, 71
- Bender R., Saglia R., Gerhard O., 1994, *MNRAS*, 269, 785
- Beuing J., Bender R., Mendes de Oliveira C., Thomas D., Maraston C., 2002, *A&A*, 395, 431
- Binney J., Merrifield M., 1998, *Galactic astronomy*. Princeton Series in Astrophysics, Princeton University Press
- Bonnet H., et al., 2004, *ESO Messenger*, 117, 17
- Caon N., Capaccioli M., D’Onofrio M., 1994, *A&A Suppl. Series*, 106, 199
- Cappellari M., et al., 2006, *MNRAS*, 366, 1126
- Corsini E. M., Wegner G., Saglia R. P., Thomas J., Bender R., Thomas D., 2008, *ApJ Suppl. Series*, 175, 462
- Davies R. I., et al., 2006, *ApJ*, 646, 754
- Davies R. I., Mueller Sánchez F., Genzel R., Tacconi L. J., Hicks E. K. S., Friedrich S., Sternberg A., 2007, *ApJ*, 671, 1388
- Davies R. I., Tacconi L., Genzel R., Ott T., Rabien S., 2004, in Bonaccini Calia D., Ellerbroek B. L., Ragazzoni R., eds, *Advancements in Adaptive Optics Vol. 5490 of Proceedings of the SPIE, Using adaptive optics to probe the dynamics and star formation in active galactic nuclei*. pp 473–482
- Davies R. L., 2000, in van Breugel W., Bland-Hawthorn J., eds, *Imaging the Universe in Three Dimensions Vol. 195 of Astronomical Society of the Pacific Conference Series, Science & Surveys with Integral Field Spectrographs (Review)*. pp 134–+
- Di Matteo T., Springel V., Hernquist L., 2005, *Nature*, 433, 604
- Eisenhauer F., et al., 2003, in Iye M., Moorwood A., eds, *Instrument Design and Performance for Optical/Infrared Ground-based Telescopes Vol. 4841 of Proc. SPIE, SINFONI—Integral field spectroscopy at 50 milli-arcsecond resolution with the ESO VLT*. pp 1548–1561
- Fabbiano G., Fasnacht C., Trinchieri G., 1994, *ApJ*, 434, 67
- Ferrarese L., Merritt D., 2000, *ApJ*, 539, L9
- Gebhardt K., et al., 2000a, *AJ*, 119, 1157
- Gebhardt K., et al., 2000b, *ApJ*, 539, L13
- Gebhardt K., et al., 2003, *ApJ*, 583, 92
- Gebhardt K., et al., 2007, *ApJ*, 671, 1321
- Geldzahler B. J., Fomalont E. B., 1984, *AJ*, 89, 1650
- Gerhard O., 1993, *MNRAS*, 265, 213

- Gössl C. A., Riffeser A., 2002, *A&A*, 381, 1095
- Goudfrooij P., Alonso M. V., Maraston C., Minniti D., 2001, *MNRAS*, 328, 237
- Goudfrooij P., Mack J., Kissler-Patig M., Meylan G., Minniti D., 2001, *MNRAS*, 322, 643
- Holley-Bockelmann K., Richstone D. O., 2000, *ApJ*, 531, 232
- Hopkins P. F., Hernquist L., Cox T. J., Kereš D., 2008, *ApJ Suppl. Series*, 175, 356
- Horellou C., Black J. H., van Gorkom J. H., Combes F., van der Hulst J. M., Charmandaris V., 2001, *A&A*, 376, 837
- Houghton R. C. W., Magorrian J., Sarzi M., Thatte N., Davies R. L., Krajnović D., 2006, *MNRAS*, 367, 2
- Iyomoto N., Makishima K., Tashiro M., Inoue S., Kaneda H., Matsumoto Y., Mizuno T., 1998, *ApJL*, 503, L31
- Johansson P. H., Naab T., Burkert A., 2008, *ApJ* submitted, astro-ph/0802.0210, 802
- Joseph C. L., et al., 2001, *ApJ*, 550, 668
- Kim D.-W., Fabbiano G., 2003, *ApJ*, 586, 826
- Kuntschner H., 1998, PhD thesis, AA(University of Durham, Department of Physics, South Road, Durham DH1 3LE)
- Kuntschner H., 2000, *MNRAS*, 315, 184
- Lauer T. R., et al., 2007, *ApJ*, 664, 226
- Longhetti M., Rampazzo R., Bressan A., Chiosi C., 1998, *A&A Suppl. Series*, 130, 267
- Lyubenova M., Kuntschner H., Silva D. R., 2008, *A&A*, 485, 425
- Mackie G., Fabbiano G., 1998, *AJ*, 115, 514
- Madore B. F., et al., 1999, *ApJ*, 515, 29
- Magorrian J., 1999, *MNRAS*, 302, 530
- Maraston C., 1998, *MNRAS*, 300, 872
- Maraston C., 2005, *MNRAS*, 362, 799
- Marconi A., Hunt L. K., 2003, *ApJL*, 589, L21
- Marconi A., Pastorini G., Pacini F., Axon D. J., Capetti A., Macchetto D., Koekemoer A. M., Schreier E. J., 2006, *A&A*, 448, 921
- Mármol-Queraltó E., Cardiel N., Cenarro A. J., Vazdekis A., Gorgas J., Pedraz S., Peletier R. F., Sánchez-Blázquez P., 2008, *A&A* accepted, astro-ph/0806.0581
- Merrifield M. R., Forbes D. A., Terlevich A. I., 2000, *MNRAS*, 313, L29
- Merritt D., 1997, *AJ*, 114, 228
- Mueller Sánchez F., Davies R. I., Eisenhauer F., Tacconi L. J., Genzel R., Sternberg A., 2006, *A&A*, 454, 481
- Neumayer N., Cappellari M., Reunanen J., Rix H.-W., van der Werf P. P., de Zeeuw P. T., Davies R. I., 2007, *ApJ*, 671, 1329
- Nowak N., Saglia R. P., Thomas J., Bender R., Pannella M., Gebhardt K., Davies R. I., 2007, *MNRAS*, 379, 909
- Oliva E., Origlia L., Maiolino R., Moorwood A. F. M., 1999, *A&A*, 350, 9
- Peletier R. F., et al., 2007, *MNRAS*, 379, 445
- Portilla J. G., Rodríguez-Ardila A., Tejeiro J. M., 2008, in *RevMexAA Vol. 32, Near Infrared (0.8-2.3μm) Coronal Lines in Active Galactic Nuclei*. pp 80–82
- Saglia R. P., Maraston C., Thomas D., Bender R., Colless M., 2002, *ApJL*, 579, L13
- Schreiber J., Thatte N., Eisenhauer F., Tecza M., Abuter R., Horrobin M., 2004, in *Ochsenbein F., Allen M., Egret D., eds, ASP Conf. Proc. Vol. 314, Data reduction software for the VLT Integral Field Spectrometer SPIFFI*. p. 380
- Schwarzschild M., 1979, *ApJ*, 232, 236
- Schweizer F., 1980, *ApJ*, 237, 303
- Schweizer F., 1981, *ApJ*, 246, 722
- Shaya E. J., et al., 1996, *AJ*, 111, 2212
- Silge J., Gebhardt K., Bergmann M., Richstone D., 2005, *AJ*, 130, 406
- Silge J. D., Gebhardt K., 2003, *AJ*, 125, 2809
- Silva D. R., Kuntschner H., Lyubenova M., 2008, *ApJ*, 674, 194
- Thomas J., Jesseit R., Naab T., Saglia R. P., Burkert A., Bender R., 2007, *MNRAS*, 381, 1672
- Thomas J., Saglia R., Bender R., Thomas D., Gebhardt K., Magorrian J., Richstone D., 2004, *MNRAS*, 353, 391
- Thomas J., Saglia R. P., Bender R., Thomas D., Gebhardt K., Magorrian J., Corsini E. M., Wegner G., 2007, *MNRAS*, 382, 657
- Tremaine S., et al., 2002, *ApJ*, 574, 740
- van der Marel R., Franx M., 1993, *ApJ*, 407, 525
- Weitzel L., Krabbe A., Kroker H., Thatte N., Tacconi-Garman L. E., Cameron M., Genzel R., 1996, *A&A Suppl. Series*, 119, 531
- Wozniak H., Combes F., Emsellem E., Friedli D., 2003, *A&A*, 409, 469
- Wright C. O., Egan M. P., Kraemer K. E., Price S. D., 2003, *AJ*, 125, 359
- Younger J. D., Hopkins P. F., Cox T. J., Hernquist L., 2008, *ApJ* accepted, astro-ph/0804.2672

APPENDIX A: DUST CORRECTION

The ground-based *Ks* band SOFI and the *H* band *HST* NICMOS imaging data were dust-corrected with according *J* band images taken with the same instruments using the following method, assuming a standard extinction law: The relation between reddening and extinction is

$$H_0 - H_c = aE_{J-H}$$

for the *HST* image (analogous for the SOFI image), where H_0 is the observed, and H_c is the dust-free image. The absorption coefficient a is defined via the extinctions in the involved bands: $a = A_{H,K}/(A_J - A_{H,K})$. For the SOFI image the values $A_J = 0.282A_V$ and $A_K = 0.112A_V$ from Binney & Merrifield (1998) were used. The NICMOS image was significantly overcorrected with A_J and A_H from Binney & Merrifield (1998). We found by iteratively changing a that the best correction is obtained for $a = 0.8$.

The observed images provide the fluxes, so with Eq. 1 it follows that

$$H_c = H_0 - a[(J - H)_0 - (J - H)_c]$$

and

$$f_{H_c} = f_{H_0} \left(\frac{f_{H_0}}{f_{J_0}} \right)^a \left(\frac{f_{J_c}}{f_{H_c}} \right)^a \propto \frac{f_{H_0}^{1+a}}{f_{J_0}^a}$$

under the assumption that $f_{J_c}/f_{H_c} \approx \text{const.}$ (i.e. approximately no intrinsic stellar population gradient). See also Beletsky et al. (2008).

APPENDIX B: DEPENDENCE OF THE RELIABILITY OF THE KINEMATICS ON INITIAL AND INTRINSIC PARAMETERS

In order to find the best value for the smoothing parameter α we performed Monte Carlo simulations on a large set of model galaxy spectra. These were created from stellar template spectra by convolving them with both Gaussian and non-Gaussian LOSVDs and by adding different amounts of noise. The results of the simulations might depend, apart from the S/N, on the spectral resolution, the LOSVD shape, the size of the velocity bins of the LOSVDs δv , the velocity range where the LOSVD is fitted Δv , the template itself or other things. Therefore we performed several sets of simulations using the best-fitting stellar template for each platescale. The spectral range $\Delta\lambda = 2.275 \dots 2.349 \mu\text{m}$ and the number of velocity bins $N = 29$ were identical for all setups. δv and Δv are given by N and the velocity dispersion σ : $\Delta v = 2 \times 4.5 \times \sigma$, $\delta v = \Delta v/N$. We created 100 model galaxy spectra for ~ 35 S/N-values between 1 and 170 and extracted the kinematics of each spectrum using MPL with ≈ 100 different values for α between 0 and 500. We tested the dependence on α for different S/N values, platescales, templates, σ , h_3 and h_4 .

B1 Dependence on S/N

The first set of simulations was done using the template star HD12642, observed on the 25mas scale. The stellar spectrum was broadened with a LOSVD with the parameters $\sigma = 250 \text{ km s}^{-1}$ and $h_3 = h_4 = 0$. Different amounts of noise were added corresponding to a S/N range of $1 \dots 170$. The kinematic parameters of the resulting spectra were recovered using the original spectrum as template star. Fig. B1 shows the results for three different S/N values. In general, the kinematics can be reliably reconstructed for a wide range of smoothing parameters ($\alpha \approx 0.5 \dots 100$ for v and h_3 , $\alpha \approx 0.5 \dots 50$ for σ and $\alpha \approx 0.5 \dots 20$ for h_4). Both σ and h_4 change slightly with α . σ is biased towards smaller values for small α and then starts to increase. h_4 is biased towards higher values for small α and continuously decreases and is biased towards smaller values for larger α . This trend is seen for all S/N. The only difference is in the error bars, they increase with decreasing S/N. For small S/N the error bars in h_4 also increase with decreasing α . As h_4 is more sensitive to changes in α than the other parameters, it can be used to determine an “optimal” smoothing parameter defined as that α where the χ^2 difference between measured and real h_4 is smallest. It is shown in Fig. B2 as a function of S/N. For $S/N \lesssim 25$ the curve shows a strong increase and then, for $S/N < 10$, large variations, meaning that it is not possible to determine reliable kinematics here. For $S/N \gtrsim 30$ the curve is smooth and decreases very slowly, a sign that the kinematics extracted from such data should be reliable.

B2 Dependence on spectral resolution and velocity template

The spectral resolution of the three platescales is slightly different, $R \approx 4500$ for the 250mas scale, $R \approx 5000$ for the 100mas scale and $R \approx 6000$ for the 25mas scale. This may have an effect on the derived kinematics or the optimal α .

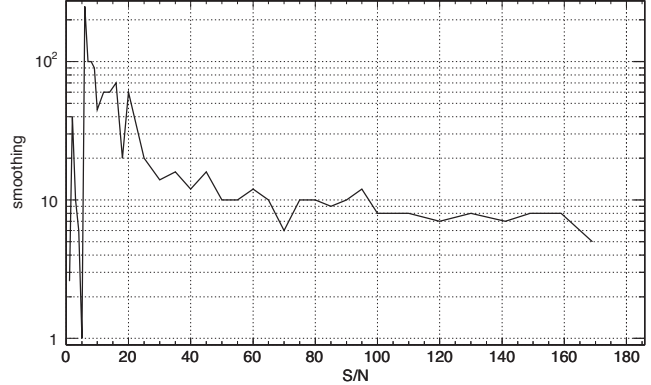


Figure B2. “Optimal” smoothing parameter as a function of S/N, derived from the minimum χ^2 between measured and real h_4 , the parameter that shows the largest variations with α . In order to derive reliable kinematics the S/N of the data should be $\gtrsim 30$.

The K5/M0III star HD181109 with a CO equivalent width of 12.9 \AA (see Tab. 1) has the largest weight in our library of velocity templates when fitting to the Fornax A spectra. This star was observed in the 100mas and 250mas scale. In the 25mas scale the K5III star HD12642 with a similar equivalent width has the largest weight. For each platescale spectra with $\sigma = 250 \text{ km s}^{-1}$, $h_3 = h_4 = 0$ and different amounts of noise as above were created using the according stellar template and the kinematic parameters were recovered with $\alpha = 0.1 \dots 500$. The results are shown in Fig. B3 for S/N= 140. No significant difference can be detected between the three platescales. Likewise the optimal smoothing parameter is equal for all platescales. Note that this set of simulations has been tailored to the Fornax A data and cannot be generalised to templates with differing CO equivalent widths and for velocity dispersions close to or below the spectral resolution.

B3 Dependence on σ

In the next set of simulations the dependence of the obtained kinematics on the velocity dispersion of the galaxy σ was tested. The spectrum of HD12642 was broadened with LOSVDs with the parameters $h_3 = h_4 = 0$ and $\sigma = 70, 120, 200$ and 250 km s^{-1} . The results are shown in Fig. B4. The kinematic parameters for all σ values show the same trends with α , but with certain differences. With decreasing σ the LOSVDs become narrower and therefore the scatter in v and σ decreases. The error bars of h_3 and h_4 are approximately constant with σ except for very low dispersions, where in addition h_4 is biased towards negative values. The reason for that could be that the velocity bin width δv is only $\approx 20 \text{ km s}^{-1}$ for $\sigma = 70 \text{ km s}^{-1}$ (i.e. smaller than the $30 \text{ km s}^{-1} \text{ px}^{-1}$ for SINFONI). For low- σ galaxies therefore more simulations are necessary to bypass this effect, preferentially with N chosen such that δv is around 30 km s^{-1} .

B4 Dependence on h_3 and h_4

With the last set of simulations we tested if the reconstructed kinematics depends on h_3 or h_4 . We created model

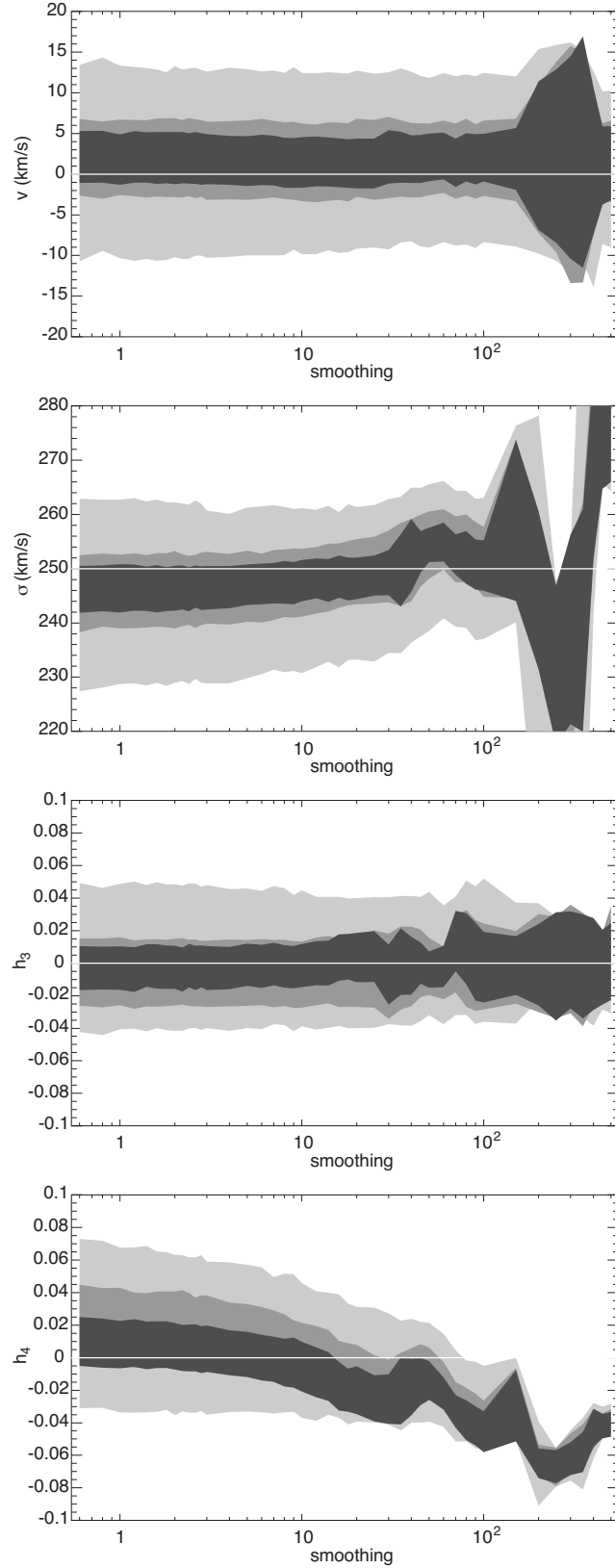


Figure B1. Kinematic parameters for different S/N (light grey: S/N=40, medium grey: S/N=90, dark grey: S/N=140). The kinematic template star HD12642 was used, observed on the 25mas scale. The spectrum was broadened using a LOSVD with $\sigma = 250 \text{ km s}^{-1}$ and $h_3 = h_4 = 0$. The reconstructed kinematics is reliable and equal for a wide range of α -values in the range of S/Ns of our data ($S/N \approx 70$ for the 250mas and the 25mas and ≈ 140 for the 100mas data on average). As expected only the error bars increase with decreasing S/N.

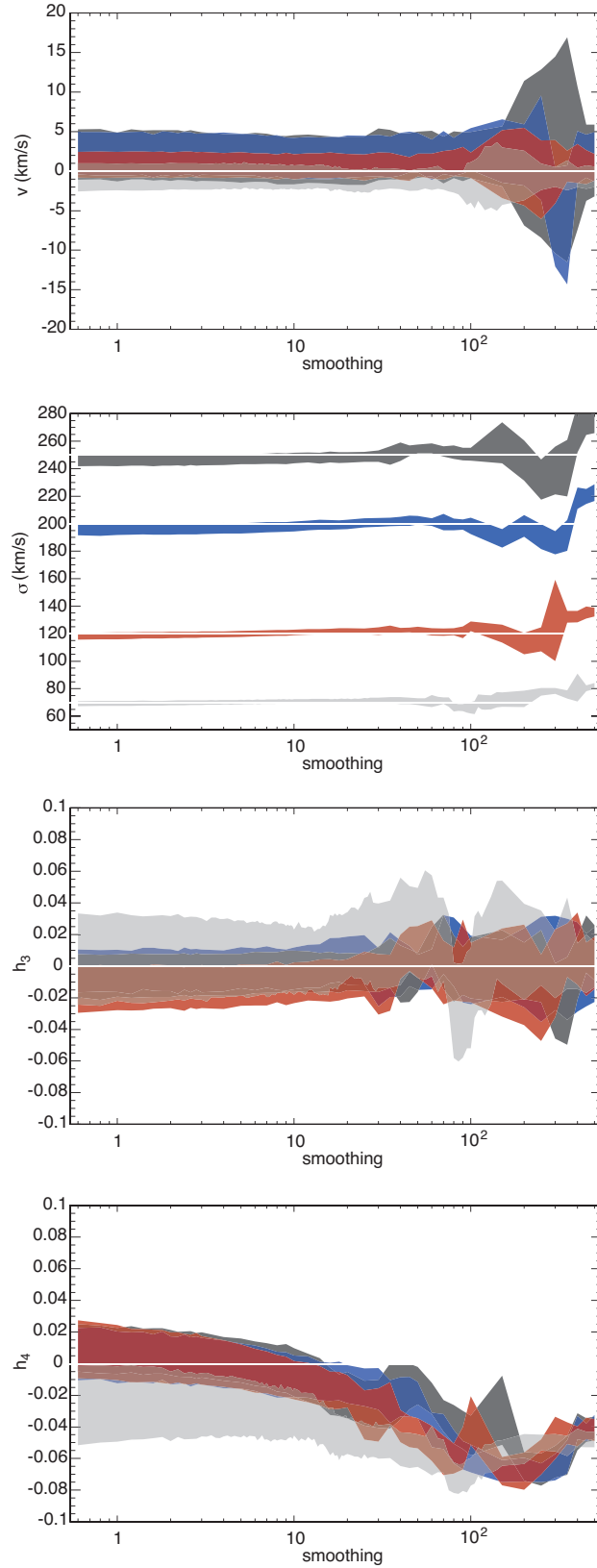


Figure B4. Kinematic parameters for different σ . Again the star HD12642 observed on the 25mas scale was used, broadened by Gaussians with $\sigma = 250$ (dark grey), 200 (blue), 120 km s⁻¹ (red) and 70 km s⁻¹ (light grey).

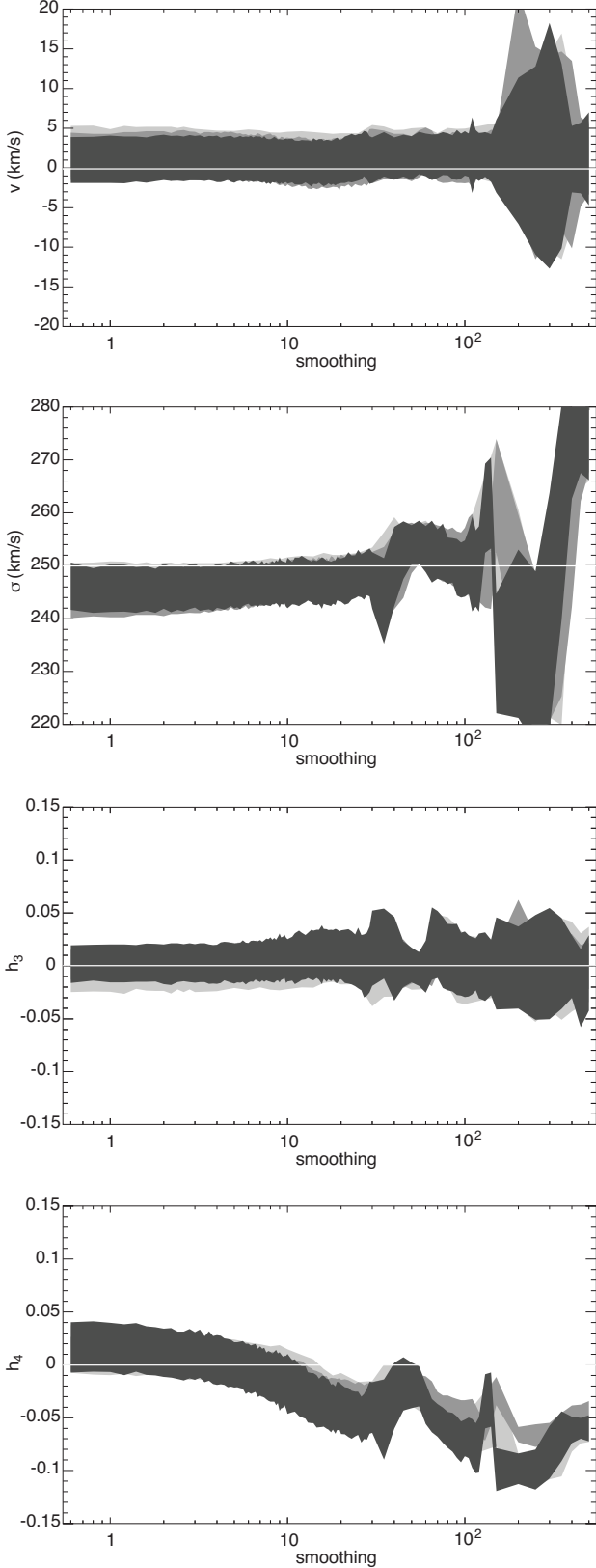


Figure B3. Kinematic parameters for the different platescales (light grey: 25mas, medium grey: 100mas, dark grey: 250mas). Here the stars HD12642 (25mas) and HD181109 (100mas and 250mas) were used, broadened by LOSVDs with $v = 0 \text{ km s}^{-1}$, $\sigma = 250 \text{ km s}^{-1}$ and $h_3 = h_4 = 0$.

galaxy spectra where h_3 and h_4 have the values -0.1 or $+0.1$ and with $\sigma = 250 \text{ km s}^{-1}$. The results are shown in Fig. B5 in comparison to the case with $h_3 = h_4 = 0$. When $h_3 \neq 0$ we find deviations from the real values with increasing α mainly in v and h_3 . For simulations with $h_4 \neq 0$ a similar behaviour is found for σ and h_4 .

B5 Results

Taking all simulations together we conclude that with MPL reliable kinematics can be obtained from the CO bandheads of the SINFONI data of Fornax A when the chosen α is between 1 and 10 and $S/N \gtrsim 30$. The S/N of our data is very high (on average 70 for the 25mas and the 250mas data and 140 for the 100mas data). We are using $\alpha = 8$ for the 25mas and 250mas data and $\alpha = 6$ for the 100mas data. These results cannot be used unrestrictedly for other datasets, especially not for different absorption lines, much lower σ close to or lower than the spectral resolution, or if the CO equivalent width is significantly different.

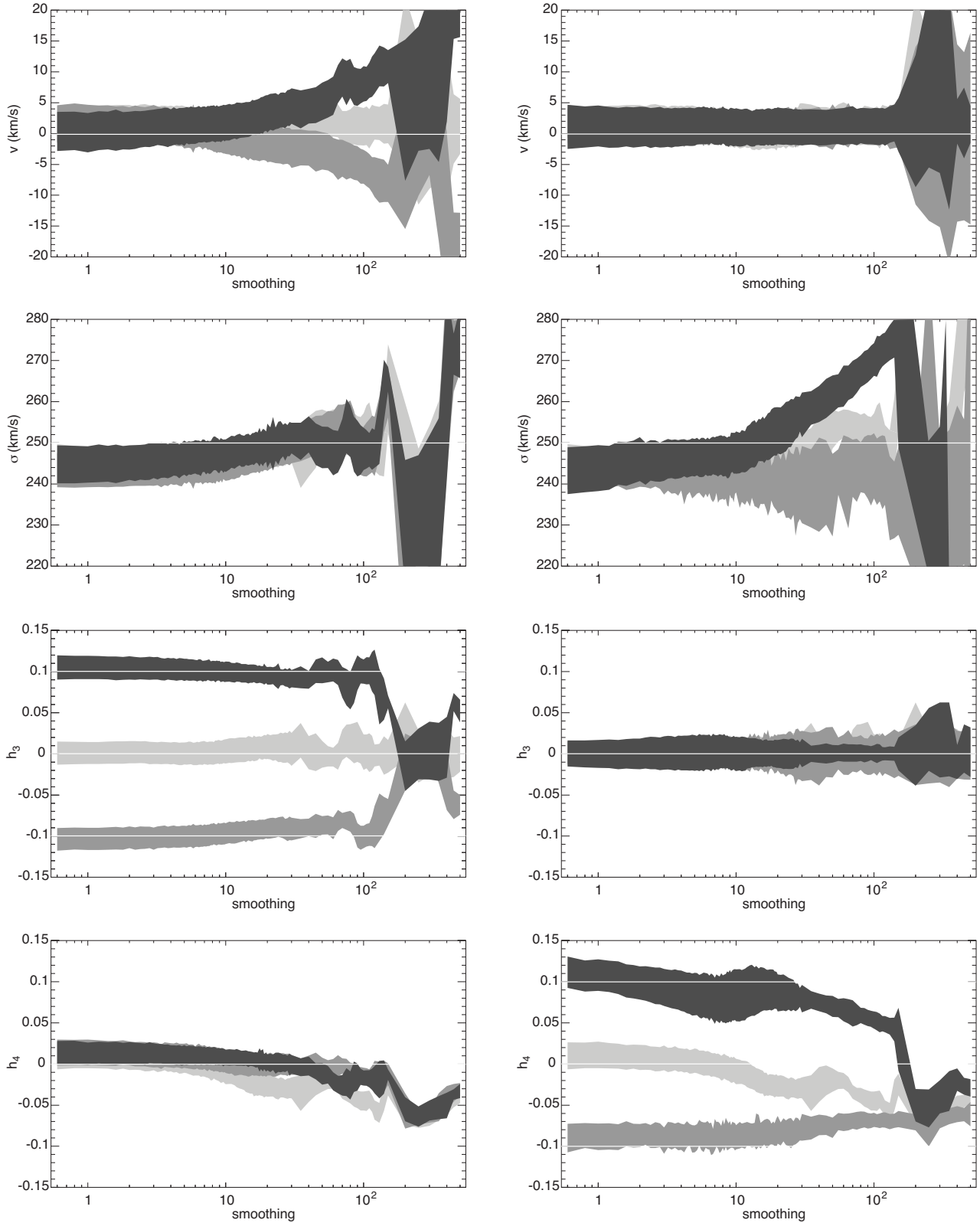


Figure B5. Kinematic parameters for different h_3 and h_4 . Here the star HD181109 observed on the 100mas scale was used. In the left column it was broadened by LOSVDs with $\sigma = 250 \text{ km s}^{-1}$ and $h_3 = -0.1$ (medium grey) or 0.1 (dark grey) and $h_4 = 0$. In the right column the stellar spectrum was broadened by LOSVDs with $\sigma = 250 \text{ km s}^{-1}$, $h_3 = 0$ and $h_4 = -0.1$ (medium grey) or 0.1 (dark grey). For comparison, the results for $h_3 = h_4 = 0$ are plotted in light grey in both columns.